PHYSICAL REVIEW APPLIED **7,** 014007 (2017)

Energy-Dependent Scintillation Pulse Shape and Proportionality of Decay Components for CsI:Tl: Modeling with Transport and Rate Equations

X. Lu, S. Gridin, and R. T. Williams[*]
Department of Physics, Wake Forest University, Winston-Salem, North Carolina 27106, USA

M. R. Mayhugh
Faceted Development, LLC, 3641 Rawnsdale Road, Shaker Heights, Ohio 44122, USA

A. Gektin
Institute for Scintillation Materials, 60 Nauki Avenue, 61001 Kharkov, Ukraine

A. Syntfeld-Kazuch, L. Swiderski, and M. Moszynski
National Centre for Nuclear Research, Andrzeja Soltana 7, PL-05-400 Otwock-Swierk, Poland

(Received 27 October 2016; revised manuscript received 8 December 2016; published 12 January 2017)

Relatively recent experiments on the scintillation response of CsI:Tl have found that there are three main decay times of about 730 ns, 3 μs, and 16 μs, i.e., one more principal decay component than had been previously reported; that the pulse shape depends on gamma-ray energy; and that the proportionality curves of each decay component are different, with the energy-dependent light yield of the 16-μs component appearing to be anticorrelated with that of the 0.73-μs component at room temperature. These observations can be explained by the described model of carrier transport and recombination in a particle track. This model takes into account processes of hot and thermalized carrier diffusion, electric-field transport, trapping, nonlinear quenching, and radiative recombination. With one parameter set, the model reproduces multiple observables of CsI:Tl scintillation response, including the pulse shape with rise and three decay components, its energy dependence, the approximate proportionality, and the main trends in proportionality of different decay components. The model offers insights on the spatial and temporal distributions of carriers and their reactions in the track.

DOI: 10.1103/PhysRevApplied.7.014007

I. INTRODUCTION

Ideally, spectroscopic scintillation detectors convert the energy of a particle stopped in the host into luminescence photons whose number is proportional to the energy of the stopped particle, so that the integrated luminescence (the detected pulse height) depends linearly on the particle energy. In real scintillators, light emission from nonlinear interactions of carriers generated in the particle track and complexities of transport and capture, along with the stochastic nature of energy deposition, introduce an energy-dependent light yield, i.e., nonproportionality. This *intrinsic nonproportionality* of real materials contributes in quadrature with other factors, including absolute detected photon number and homogeneity of light collection, to determine the energy resolution [1–3]. Gamma-ray energy resolution is of practical importance for element and isotope screening in security applications, well logging, and certain medical applications as well as spectroscopy in physics experiments [4–6]. One hopes to discover and/or engineer a scintillator with both a high absolute light yield and a plot of light yield versus energy (proportionality curve) that is as flat as possible.

Besides proportionality, scintillators are also characterized by measuring their pulse rise and decay times. The rise time is important for event timing, with notable applications to time-of-flight positron-electron tomography [7] in medicine and extracting data from multiple collisions per bunch in the next-generation high-luminosity Large Hadron Collider experiments [8], for example. The decay time is important to the maximum event rate with respect to the pulse pileup. The decay in different scintillators can be described as single exponential, multiple exponential, or nonexponential. In deference to the last two, one may more properly speak of the decay curve rather than decay time, including information on relative amplitudes of the decay components. It is common to refer to the *pulse shape* representing both rise and multicomponent decay. One might suppose that a single short decay would be preferred, but a multicomponent decay curve whose shape depends on ionization density enables pulse-shape discrimination between gamma-ray and massive (e.g., proton, alpha) particle events and is especially valuable for neutron and gamma discrimination in detectors. Extra information about the ionization track coded in the pulse shape could potentially improve energy resolution [9–11].

---

[*] williams@wfu.edu

Direct experimental evidence that proportionality and pulse shape can be intertwined includes the gamma energy dependence of decay times in CsI:Tl [12] and the recent measurement of different proportionality curves for each decay-time component in CsI:Tl [13]. This paper presents computational modeling aimed at duplicating the pulse shape, including its energy dependence and the corresponding separate proportionalities of decay components. This modeling leads to insight on the scintillation processes involved.

The transport- and rate-equation model that we use to fit and analyze these experiments was used earlier to calculate the proportionality of the total light yield as well as time- and radial-space-resolved distributions of the participating carriers and trap populations in the system of undoped CsI at two temperatures (295 and 100 K) and CsI with Tl dopant at room temperature [14]. A brief review of the model and enhancements made for the analysis in this work, primarily the reporting of scintillation pulse shape, is given in Sec. II. The seven-equation base model employed here is the same as the one used in Ref. [14]. There are changes in some of the material-specific rate coefficients, mainly the bimolecular recombination rate constants involving the Tl activator in CsI:Tl (B_{et} and B_{tt}) and the linear rate constant (S_{1h}) for self-trapped-hole capture on Tl^{+}.

II. OVERVIEW OF THE MODEL

Our computational model of scintillation was described in Ref. [14]. Starting with a specified ionization density deposited initially in a track of an assumed cylindrical Gaussian profile, the recombination portion of the model calculates the fraction of this ionization that produces photon emission. The computation is performed using the coupled rate and transport equations listed in Eqs. (1)–(7) below, evaluated by a finite-element method. The seven equations listed below are mathematically the same as those used in Ref. [14], but we choose a different naming of factors comprising the coefficients of the terms involving Tl-trapped electrons that become temporarily mobile when thermally ionized. For reasons of computational efficiency explained in Ref. [14], we had constructed a diffusion coefficient, mobility, and defect-trapping rate constant for electrons trapped in equilibrium on Tl as follows: $D_{et} = (U_{et}/S_{1e})D_e$, $\mu_{et} = (U_{et}/S_{1e})\mu_e$, and $K_{1et} = (U_{et}/S_{1e})K_{1e}$, where the subscript *et* indicates a coefficient for Tl-trapped electrons and *e* alone indicates corresponding coefficients for conduction electrons that have not yet entered the cycle of trapping, release, and retrapping on Tl. The trapping and recapture of electrons on thallium is treated as if diffusion of Tl^0 were taking place, saving the need to continue executing femtosecond time steps to deal with conduction electrons into the microsecond range, where essentially all carriers are in equilibrium with traps, as will be seen in this study to be the case. U_{et} is the rate constant for untrapping an electron from Tl^0 and S_{1e} is the rate constant for trapping an electron on Tl^{+} to form Tl^0. Thus, the ratio (U_{et}/S_{1e}) describes the fraction of time that an electron bound in Tl^0 at thermal equilibrium spends in the conduction band, able to respond to electric fields and gradients as well as to participate as the mobile species in recombination with Tl^{2+}-trapped holes or capture on other defects. In Ref. [14], we introduced D_{et}, μ_{et}, and K_{1et} as new material parameters, even though they are scaled by the fixed ratio (U_{et}/S_{1e}) relative to the free-electron parameters D_e, μ_e, and K_{1e}. Writing the same equations now with an explicit display of the ratio $U_{et}/S_{1e} = f_e$ (for "free-electron fraction") avoids the introduction of apparently new material parameters for the activator-doped material that are simply scaled from host parameters that have already been used. For B_{tt}, defined in Ref. [14] as the bimolecular rate constant for electrons from Tl^0 combining with holes trapped as Tl^{2+}, we introduce B_{tt}^0 in the new display format where $B_{tt} = f_e B_{tt}^0$. The remaining symbols and terms in the equations and relevant aspects of the solution method are as described in Ref. [14]:

$$\frac{dn_e}{dt} = G_e + D_e\nabla^2 n_e + \mu_e\nabla\cdot n_e\vec{E} - (K_{1e} + S_{1e})n_e - Bn_en_h - B_{ht}n_en_{ht} - K_3n_en_en_h - K_3n_en_en_{ht} \tag{1}$$

$$\frac{dn_h}{dt} = G_h + D_h\nabla^2 n_h - \mu_h\nabla\cdot n_h\vec{E} - (K_{1h} + S_{1h})n_h - Bn_en_h - B_{et}n_{et}(1-f_e)n_h - K_3n_en_en_h - K_3n_en_{et}n_h \tag{2}$$

$$\frac{dN}{dt} = G_E + D_E\nabla^2 N - (S_{1E} + K_{1E})N - R_{1E}N + Bn_en_h - K_{2E}N^2 \tag{3}$$

$$\frac{dn_{et}}{dt} = D_e\nabla^2 n_{et}f_e + \mu_e\nabla\cdot n_{et}f_e\vec{E} + S_{1e}n_e - K_{1e}n_{et}f_e - B_{et}n_{et}(1-f_e)n_h - B_{tt}^0n_{et}f_en_{ht} - K_3n_en_{et}n_h \tag{4}$$

$$\frac{dn_{ht}}{dt} = D_{ht}\nabla^2 n_{ht} - \mu_{ht}\nabla\cdot n_{ht}\vec{E} + S_{1h}n_h - K_{1ht}n_{ht} - B_{ht}n_en_{ht} - B_{tt}^0n_{et}f_en_{ht} - K_3n_en_en_{ht} \tag{5}$$

$$\frac{dN_t}{dt} = S_{1E}N - R_{1Et}N_t + B_{ht}n_en_{ht} + B_{et}n_{et}(1-f_e)n_h + B_{tt}^0n_{et}f_en_{ht} - K_{2Et}N_t^2 \tag{6}$$

$$S_{1x} = \frac{n_{\mathrm{Tl}^+}}{n^0_{\mathrm{Tl}^+}} S^0_{1x}, \tag{7}$$

where $n_{\mathrm{Tl}^+} = n^0_{\mathrm{Tl}^+} - n_{et} - n_{ht} - N_t$.

The radiative rates, $R_{1Et}N_t$ from an excited Tl^{+*} and $R_{1E}N$ from self-trapped excitons (STE), are evaluated from a solution of the coupled equations for all populations as a function of time starting from an initial on-axis excitation density n_0. The time-integrated radiative rate gives the corresponding light output. Division of the total light output by the total number of initial electron-hole pairs at the initial excitation density being considered gives the light yield as a function of the initial ionization density. We call this intermediate result the local light yield, $Y_L(n_0)$. The calculation is repeated for a number of excitation densities.

In the energy-deposition part of the model calculation, GEANT4 Monte Carlo simulations [15] are used to record the energy and track length for each subevent making up the total deposition by a monoenergetic electron of initial energy E_i. From such simulations, the ionization density (e-h/cm^3) can be determined for every parcel of energy deposited based on the dE/dx so calculated and the assumed Gaussian radial profile of the track having an initial radius r_0, which is a parameter of the model. The calculations of the local light yield are carried out for a range of ionization densities that span the GEANT4 results.

Introduction of a radial profile of some kind is essential on dimensional grounds to convert the rate of linear energy deposition dE/dx (eV/nm) to units of deposited carrier density (e-h/cm^3) in terms of which the kinetic rate and transport equations are defined. The conversion is written as

$$n_0 = \frac{dE/dx}{\pi r_0^2 \beta E_{\mathrm{gap}}}, \tag{8}$$

where r_0 is the $1/e$ radius of the track profile expressed as $\exp(-r^2/r_0^2)$ in Ref. [16] and βE_{gap} is the average energy invested per electron-hole pair created. Using this conversion and the GEANT4 simulations yields a probability of occurrence of each excitation density n_0 during the stopping of a primary electron of initial energy E_i, written as $F(n_0, E_i)$. In the calculations of Ref. [14], an average probability function $F_{\mathrm{av}}(n_0, E_i)$ was constructed from 100 to 2000 GEANT4 simulations at each initial electron energy, whereas, in this work, the single-simulation probability function $F(n_0, E_i)$ is used to calculate and store 100 to 2000 light yields of simulated single events, which can be averaged at the end. Given the same set of simulated events, the averaged light-yield results are the same for both methods. The approach adopted here is well suited for the simulation and analysis of pulse-height spectra in future work.

Having both $F(n_0, E_i)$ from GEANT4 simulations and the local light yield $Y_L(n_0)$ from the solution of Eqs. (1)–(7), the formal calculation of light yield as a function of initial energy (i.e., electron response or proportionality) is obtained by integrating the product $F(n_0, E_i)Y_L(n_0)$ over n_0. We have used an interpolation procedure in this step. Fifteen or so local light-yield calculations, $Y_L(n_0)$, are used as a framework to interpolate the light response for each parcel of excitation density, and the contributions from all such parcels are summed to give the scintillator's response to that electron.

For the study of rise and decay times in this work, the $Y_L(n_0)$ values are recorded for all excitation densities at times of interest during the initial calculation. Subsequently, the response at each time can be calculated. Repeating the process at various times gives the signal as a function of time for the initial electron energy under consideration. Completing the calculation for all modeled energies gives the pulse shape for each energy and proportionality as a function of time.

In Eq. (6) above, the population of the excited activator, Tl^{+*}, is denoted by N_t, meaning "exciton trapped on activator." Similarly, the density of self-trapped holes [STH] is n_h, and the density of thallium-bound electrons [Tl^0] is n_{et}. The term $B_{et}n_{et}(1-f_e)n_h$ (which approximately equals $B_{et}n_{et}n_h$) governs the moderately fast bimolecular formation of Tl^{+*} by the well-known reaction $\mathrm{STH} + \mathrm{Tl}^0 \rightarrow \mathrm{Tl}^{+*}$. The $B^0_{tt}n_{et}f_e n_{ht}$ term governs the slower process involving trapped electron release from Tl^0, followed by capture of the electron on Tl^{2+} that had been formed by prior hole capture (at the rate $S_{1h}n_h$), to also produce an excited activator, Tl^{+*}. The following sections will refer especially to the three parameters B_{et}, B^0_{tt}, and S_{1h}, which have critical roles in determining the pulse shape in CsI:Tl. Thus, fitting the pulse shape presents an opportunity to refine their values before addressing proportionality and total light yield.

The model of Ref. [14] was developed and tested for electron proportionality (relative light yield versus electron energy), and it is used in this work to compare with gamma-ray proportionality data [12,13]. Swiderski *et al.* [17] have compared electron response and gamma response of CsI:Tl from about 30 keV to 1 MeV. With a 12-μs shaping time, the differences between gamma and electron response over this energy range are modest, so we believe the comparisons being made in this work are informative and support useful conclusions about mechanisms of both electron and gamma response. In a forthcoming work, we will model gamma proportionality and the pulse-height spectrum directly.

III. PULSE SHAPE AND ITS ENERGY DEPENDENCE

A. Experimental data

Syntfeld-Kazuch *et al.* [12] measured the pulse shape of CsI:Tl (0.06%), excited at several gamma-ray energies between 662 and 6 keV using a so-called slow-slow single-photon method described in Refs. [18] and [19], tailored to reduce the background of random coincidences. With this method, they were able to resolve a "tail" decay component of about 16 μs in addition to the "fast" and "slow" components of 730 ns and 3.1 μs reported in prior studies of CsI:Tl scintillation decay [20,21]. The pulse shapes for 662- and 6-keV gamma excitation measured in Ref. [12] are plotted in Fig. 1. The 16-μs tail accounts for about 22% of the integrated pulse for 662-keV excitation, compared to 48% and 30% for the fast and slow components, respectively [12]. Decay curves of scintillation from 16.6-, 60-, 122-, and 320-keV gamma rays were also measured in Ref. [12], reported in terms of fitted exponentials and their amplitudes.

The decay times of 730 ± 30 ns, 3.1 ± 0.2 μs, and 16 ± 1 μs are determined by fitting the decay curve for 662-keV excitation [12]. The corresponding decay times under 6-keV excitation are 670 ± 20 ns, 3.1 ± 0.3 μs, and 14 ± 3 μs, indicating that the fast and tail decay times decrease slightly with decreasing gamma energy. Noting that there is only a weak dependence of the fitted decay times upon gamma-ray energy, the authors of Ref. [12] presented data on how the relative amplitudes (the integrated intensities) of the fast, slow, and tail decay components changed in six gamma energy steps from 662 to 6 keV. A main conclusion of their study was that the fast-to-tail ratio increases as gamma excitation energy is lowered. Fitting the observed pulse shape as a function of energy and understanding the physical origins of the decay components are among our objectives in this work.

The data in Fig. 1 are a multichannel analyzer record of times from start to single-photon stop events which samples the scintillation lifetime and is adjusted with delays to put the start time for the pulse on scale. This adjustment ensures that the data records shown in Fig. 1 show a rising portion of the curve within the stated 20-ns experimental resolution in Ref. [12]. However, the measurement method itself does not specify a time zero. The rise to a peak and initial decay out to 2.5 μs are shown on an expanded time scale in the inset of Fig. 1. Syntfeld-Kazuch *et al.* [12] normalized their data at the peak for display, and we will follow their lead in making comparisons to the model. The time zero in the model is definite, corresponding to the initial energy deposition, and can be read from the model curve matched to the experiment curve at its peak. The curves in both the main figure and the inset of Fig. 1 are normalized and presented, with the peak intensities coinciding in time and amplitude. The red and blue traces in the inset are for 662 and 6 keV excitations measured by Syntfeld-Kazuch *et al.* in an experiment optimized for weak signals at long times [12,18,19]. We have also examined 511-keV excitation data measured by Valentine *et al.* [20] in an experiment optimized for fast response at the expense of resolving slow, weak signals.

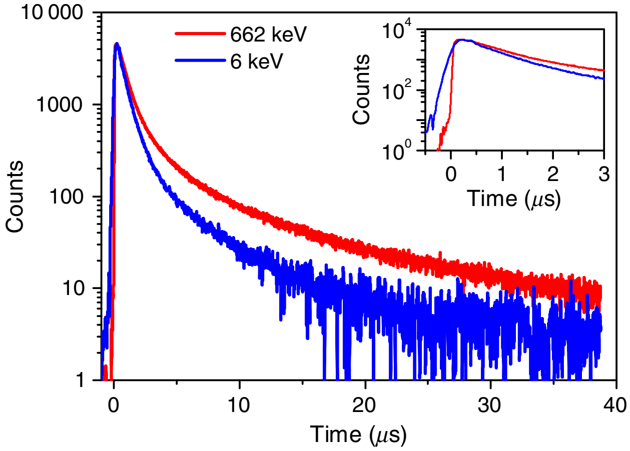

FIG. 1. Experimental pulse rise and decay over the full measured range 0–40 μs in CsI:Tl from Ref. [12] is shown for 662-keV gamma excitation in the red trace and for 6-keV gamma excitation in the lower blue trace.

Many previous studies [20–23] have associated the approximately 700-ns fast decay mainly with the reaction STH + Tl^0, and the approximately 3-μs slow decay with electrons thermally released from Tl^0 recombining with Tl^{2+} that are formed by STH capture at Tl^+ dopants. This association of the two main physical recombination routes involving STH and Tl^{2+}, respectively, with the decay components seems complete when there are only two decay components known experimentally (other than what is considered afterglow). With three identifiable decay components having roughly similar integrated strengths that are now known [12], an assessment of the responsible physical mechanisms seems in order.

Our underlying model accounts for the trapping of both electrons and holes by Tl^+ in the lattice. Carriers created by high-energy radiation are initially hot, with excess kinetic energy. As a result, electrons created in CsI spread quickly to a mean radius of about 50 nm (extending as far as 200 nm) [24], and they are trapped with a $1/e$ time of approximately 3 ps [14,25] by Tl^+ to form Tl^0. Self-trapping of the coproduced holes is commonly presumed to localize them initially at the original track. The transport and recombination kinetics of these STH with the Tl-trapped electrons (denoted Tl^0) initially governs the formation of excited Tl^{+*}'s that are responsible for scintillation light. Together with the Tl^{+*} photoluminescence decay time of 575 ns, these transport and recombination kinetics determine the finite rise time and the 730-ns fast decay time of scintillation in CsI:Tl. In parallel, the STH are competitively trapped on Tl^+, accumulating a population of Tl-trapped holes (Tl^{2+}) until all STH are exhausted by these two channels. With appropriate proximity and the thermal untrapping of electrons from Tl^0, this Tl^{2+} population, considered deeply trapped and immobile, recombines with the electrons released from Tl^0 to produce Tl^{+*} at longer times. For these calculations, we adopt the conventional assumption that it is the electron that is untrapping from Tl^0. An alternative suggestion that Tl^0

is a deep electron trap [26–28] and that holes instead untrap thermally from Tl^{2+} to recombine with the static Tl^0 has been made [26].

B. Model results: Fitting rise and decay times

The 662-keV pulse-shape data reported in Ref. [12] are reproduced by the red trace with noise in Figs. 2(a) and 2(b). The smooth curve superimposed shows the simulation of Tl^{+*} emission calculated by the model described in Sec. II with material input parameters to be tabulated and discussed later in this paper.

The experimental data and model calculation for a 662-keV excitation is shown on a log scale versus linear time out to 5 μs in Fig. 2(a). Superimposed is a 575-ns exponential representing the decay time measured for UV-excited Tl^{+*} photoluminescence in CsI:Tl at room temperature by Hamada *et al.* [21]. It has been shown that Tl photoluminescence in CsI exhibits four bands, and the dominant visible luminescence at room temperature (2.25 eV) has been attributed to a STE perturbed by substitutional Tl^+ on an adjacent site [29]. In the present modeling at room temperature, we approximate it simply as one excited state with 575-ns photoluminescence decay time, called by the short name Tl^{+*}. Future studies may examine whether the complexity of the Tl emission center itself further complicates the scintillation decay, such as how the various energy minima of the excited state are populated in the scintillation process. The observed scintillation decay is slower than 575 ns, as can be seen in the figure and as many others have observed. As discussed by other authors [20–22,30], the main mechanism for the formation of Tl^{+*} in the first 200 ns or so is the hopping diffusion and capture of STH on Tl^0 sites formed much earlier by rapid electron capture on Tl^+. For the scintillation decay to be longer than the 575-ns photoluminescence decay time, the excited Tl population should be fed while it also undergoes radiative decay. This formation process also accounts for the initial rise characteristics.

In Fig. 2(b), the model calculation with the same parameters is compared to the full range of the experimental 662-keV scintillation decay out to 40 μs. In Ref. [12], raw data with noise and the rise to a peak before decay were shown only for the 662- and 6-keV gamma energies. However, decay data for the six gamma energies 662, 350, 122, 60, 16.6, and 6 keV were reported as a set of three fitted exponential decay times, and the amplitude of each [12]. We reconstruct the decay curves shown in Fig. 3 from the experimentally determined decay constants and amplitudes reported in Ref. [12]. The experimental curves for 662, 350, and 122 keV overlap, so what is seen in Fig. 3

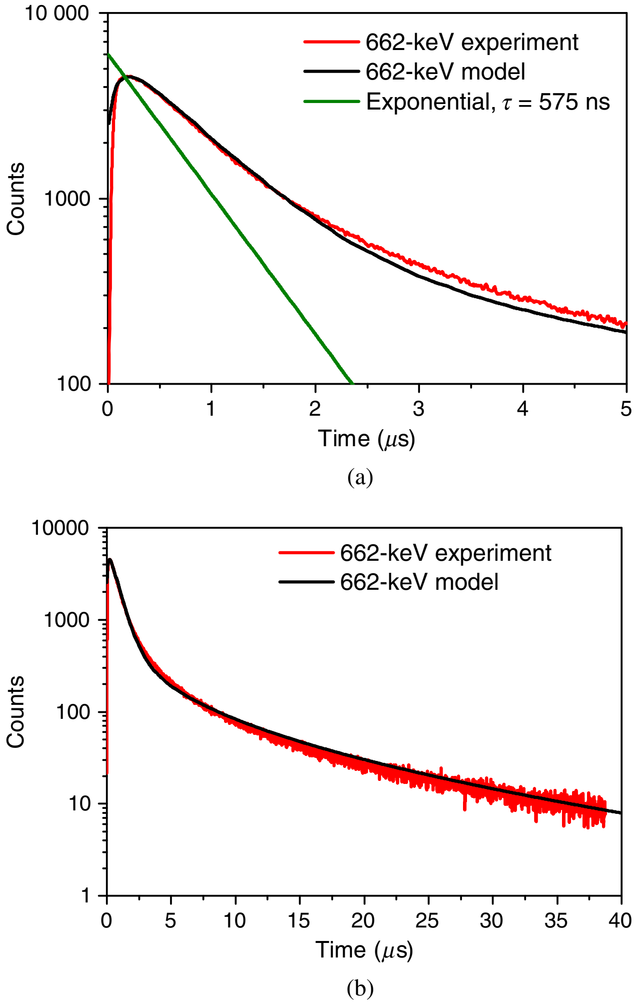

FIG. 2. Experimental scintillation decay curve from Ref. [12] for 662-keV gamma excitation shown by red traces with noise on (a) (0–5)-μs time scale and (b) (0–40)-μs scale. In both cases, the superimposed smooth black line is the modeled light output for a 662-keV excitation. The model is normalized to the experiment at the peak.

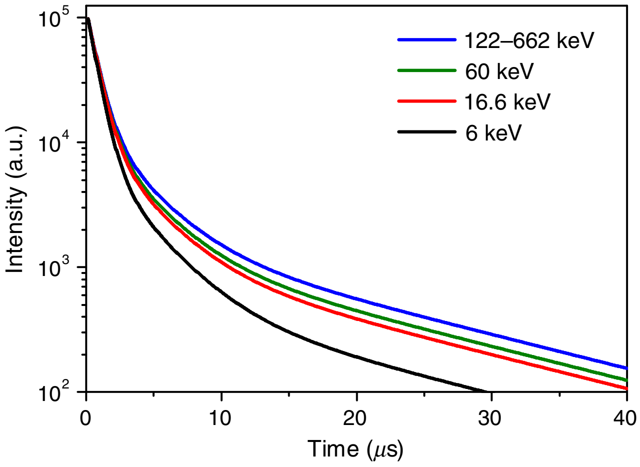

FIG. 3. Reconstructions of measured scintillation decay curves for six gamma-ray energies in CsI:Tl (0.06%) based on the time constants and integrated amplitudes reported in Ref. [12]. Only the decay curves are represented. The curves for 122, 320, and 662 keV overlap in the top curve.

is a single curve labeled 122–662 keV at the top, with three curves below it corresponding to 60, 16.6, and 6 keV, respectively. There is no representation of the early rise to a peak. These reconstructed decay curves are normalized to a value 10^5 at $t = 150$ ns, which corresponds to the peak of the intensity curve in the model results.

The modeled light output curves are shown in Fig. 4 for gamma energies of 662, 350, 122, 60, 16.6, and 6 keV. The curves are normalized to 10^5 at 150 ns, the peak of light output. We do not display all of the experimental and modeled curves in a single figure because it would be hard to distinguish them. Except for the 6-keV curve, the pulse shape is similar in the model and the experiment. As we discuss in Sec. VII, we do not try to make an exact fit with many free parameters, but we revise as few material input parameters as possible relative to Ref. [14]. As a result, some of the remaining differences between Figs. 3 and 4 are probably attributable to input parameter values that are not yet fully correct, though deficiencies in the model itself cannot be ruled out. For example, the experimental curves in Fig. 3 are more rounded in the range of 3–5 μs than are the simulated curves of Fig. 4. The common trend of an increasing peak-to-tail ratio with a decreasing energy is displayed in both the simulation and the experiment.

There is disagreement in the amount of tail amplitude change (relative to the peak of the fast component amplitude) between the model and the experiment at the lowest excitation energy, 6 keV. In the model, the depression of the relative tail amplitude continues at a rate consistent with the trend at higher energies, but the tail amplitude in the experiment drops a great deal more between 16.6 and 6 keV than at any other energy interval, and it thus differs from the model. One possible reason for the disagreement between the experiment and the model at very low gamma energy is a known difficulty of light-yield and decay-time studies when the excitation occurs near the surface. A 6-keV gamma or x ray has an attenuation length of about 3.6 μm in CsI. This value is within the range of the surface in which quenching effects have often been reported [31,32]. Such effects could be expected to affect the long tail of excitation decay more severely than the fast component because a longer time interval allows more diffusion toward the surface and allows quenching to occur. The amplitude of the tail could be decreased and its apparent decay time shortened because of the competing channel for deexcitation presented by quenching centers near the surface.

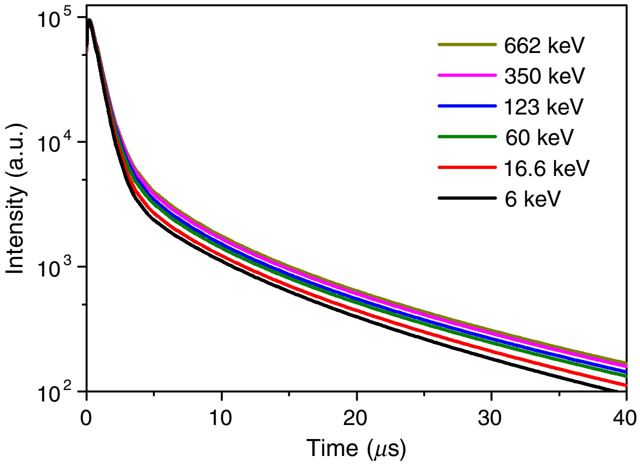

FIG. 4. Decay curves calculated from the model for six electron energies of the same values as the gamma energies of the reconstructed experimental decay curves in Fig. 3.

The model curves shown in Fig. 2 reach a peak at about 200 ns, matching the measurements in Ref. [33], which used methods chosen to reduce random coincidences [19] at some sacrifice of rise-time resolution. Rise and peaking data for CsI:Tl were reported by Valentine *et al.* with better time resolution [20]. Their data include an ultrafast component that can be aligned with the rise of the calculated STE emission in the model curve. Comparison on that basis indicates that the experiment reaches its peak 50–100 ns sooner than the results fitted to the Syntfeld-Kazuch *et al.* measurement [12]. Hamada *et al.* [21] report decay data for samples with Tl content from 10^{-2} to 10^{-6} and their rise time ranges from 100 to 185 ns, respectively. As commented earlier, these alternate fast-time data sets do not include decay data to long times (20–40 μs), so we concentrate on fitting the full set of data from Syntfeld-Kazuch *et al.* [12]. The contribution of STE luminescence is not plotted in Fig 2. The STE contribution to luminescence at room temperature is very small compared to the Tl^{+*} emission except for the details of the initial rise that occur within the 20-ns resolution of the experimental data now being compared. It is known from experiment that the STE in CsI at room temperature is thermally quenched to about 2% yield coming as a 15-ns emission from an equilibrated type-I–type-II STE configuration [32].

IV. NONPROPORTIONALITY OF EACH DECAY COMPONENT: EXPERIMENTAL DATA AND MODEL RESULTS

The proportionality curves for the fast, tail, and total decay components in CsI:Tl (0.06%) were reported by Syntfeld-Kazuch *et al.* [13] in 2014, following the method developed in Ref. [34], and are replotted below in Fig. 5(a). The experimental proportionality curves for decay components in Fig. 5(a) are determined by fitting the measured decay curve at each gamma energy to 730-ns, 3-μs, and 16-μs components and plotting the integrated light yield in each component versus the gamma energy, normalized at 662 keV.

Figure 5(b) plots the calculated proportionality curves for the fast (730 ns) and tail (16 μs) components, as well as the total pulse proportionality in CsI:Tl (0.06%), using the model of Eqs. (1)–(7) [14] and the same parameters that produced the preceding fits of the pulse-shape data. We emphasize that the calculated proportionality curves in

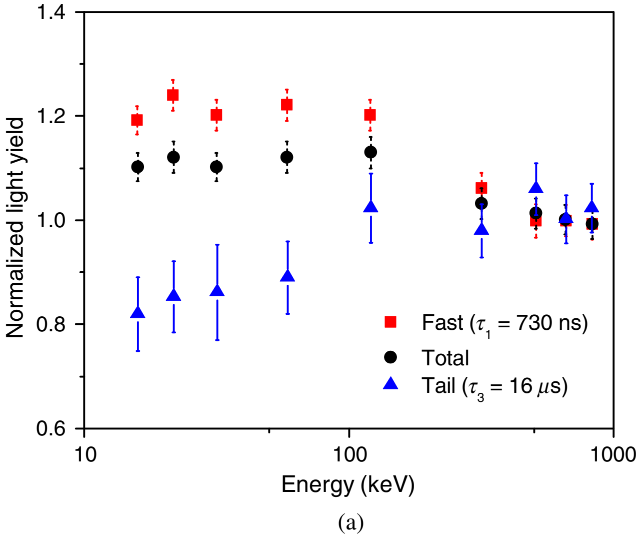

(a)

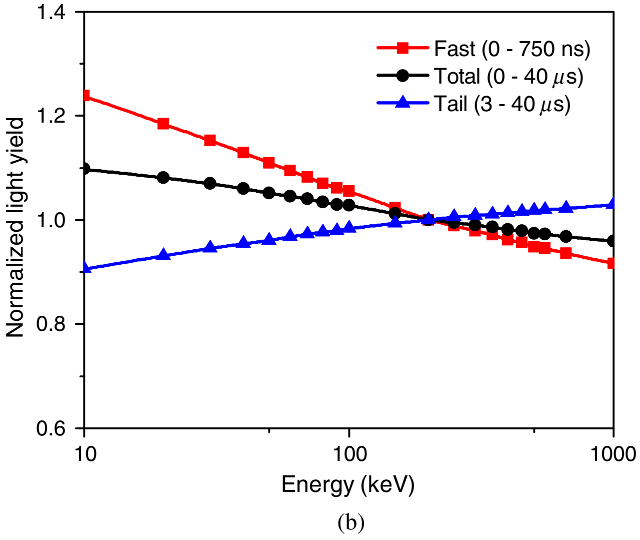

(b)

FIG. 5. (a) Experimental proportionality curves for the fast (0.73 μs) and tail (16 μs) decay components, as well as the proportionality of the total emission [Fast + Slow ($\tau_2 = 3\ \mu$s) + Tail] in CsI:Tl are plotted versus the gamma-ray energy. Reproduced from Ref. [13]. (b) Simulated proportionality curves for fast, total, and tail decay components in CsI:Tl calculated with the same model and parameter set used in Figs. 2 and 4. The integration gate intervals for the three decay components are given in the legend. The model curves are normalized at 200 keV for reasons discussed in Ref. [14].

Fig. 5(b) come directly out of the model, with its parameter set refined to give good fits to the rise and decay data, without any further fitting to reproduce the proportionality curves of separate decay components.

The approximate proportionality curves for specified decay times in Fig. 5(b) were calculated from the model output in the following way. The integrated light emission from 0 to 750 ns is plotted as the fast light yield versus electron energy; from 750 ns to 3 μs as the slow light yield versus energy; from 3 to 40 μs as the tail light yield versus electron energy; and from 0 to 40 μs as the total light yield versus energy. We are comparing proportionalities of decay components calculated by a simulated gating time method with experimental proportionalities of decay components analyzed as integrated strengths of three fitted exponential components. There should be qualitative and reasonable quantitative correspondence between the two methods. Qualitative correspondence is what we are pointing out in Fig. 5. The modeled proportionality curves are normalized at 200 keV for reasons discussed in Ref. [14]. It is a consequence of the approximate energy range over which the cylinder approximation of the track is valid.

V. ORIGIN OF THREE DECAY COMPONENTS OF SCINTILLATION IN CSI:TL

Two particularly intriguing questions are posed by the experimental observations reviewed in Secs. III A and IV. (a) To what can the three main decay components of 0.73, 3.1, and 16 μs in CsI:Tl be attributed? (b) To what can the different proportionality curves for the three decay components, particularly the anticorrelation of fast and tail components, be attributed? We address the origin of the three decay times first.

A. Recombination reactions resulting in Tl^{+*} light emission in CsI:Tl

Beginning with Dietrich *et al.* [22] and in many works since [20,23], four main recombination processes have been considered as contributors to CsI:Tl scintillation. Reaction 1 comprises direct Tl^{+} excitation and/or prompt electron- and free-hole capture on Tl^{+} to contribute a promptly rising signal that should decay at the 575-ns photoluminescence decay time of Tl^{+*}. However, this pure 575-ns decay is rarely distinguishable from the stronger 730-ns “fast component” of CsI:Tl scintillation commonly attributed to reaction 2—self-trapped holes recombining with electrons on Tl^{0}, $\mathrm{STH} + \mathrm{Tl}^{0} \rightarrow \mathrm{Tl}^{+*}$. Reactions 1 and 2 together should contribute to the observed fast scintillation decay, with reaction 2 ($R2$) dominant, because the self-trapping of holes is very fast, and hot electrons disperse and form Tl^{0} that is mostly separated from the STH in the track core.

As reviewed in the Introduction and elsewhere [14,20–23,35], the generally accepted reaction 3 in CsI:Tl is the thermal release of electrons trapped early in the track formation as Tl^{0}, followed by diffusion through repeated release and recapture until recombination with a hole trapped as Tl^{2+}. For a shorthand label, we refer to $\mathrm{Tl}^{0} + \mathrm{Tl}^{2+} \rightarrow \mathrm{Tl}^{+*}$ as reaction 3. This reaction has been considered responsible for the single observed slow component of roughly 3 μs seen in works prior to Ref. [12], e.g., as reviewed by Valentine *et al.* [20]. Kerisit *et al.* noted that the 3-μs time range brackets the decay time of Tl^{0} due to electron release at room temperature, approximately

1.8 μs [36], and associated the single time constant τ_e (for electron release from Tl^0) with the scintillation decay time of approximately 3 μs [23].

Reaction 4 involving Tl in alkali halide scintillators is $STE + Tl^+ \rightarrow Tl^{+*}$, i.e., self-trapped excitons migrating to encounter substitutional Tl^+ and transferring their excitation to create Tl^{+*}. Murray and Meyer [35] suggested this STE reaction channel as having the main responsibility for scintillation in NaI:Tl. However, following subsequent time-resolved kinetic studies on KI:Tl with a partial extension to NaI:Tl, Dietrich *et al.* later concluded that "… nearly all (approximately 95%) of the energy transport takes place by electron-hole diffusion" [22]. The computational model used herein takes into account very rapid spatial separation of hot electrons relative to self-trapped holes [24] and the effect of rapid electron trapping on Tl^+ directly measured by picosecond spectroscopy [25]. These effects hinder the formation of STEs in Tl-doped CsI relative to undoped CsI, where the line of holes draws free conduction electrons back to the track after they thermalize [14]. STEs that form in CsI:Tl despite the fast competing channels of carrier capture on Tl must then survive thermal quenching at room temperature [32] in order to finally excite Tl^+. The model calculations indicate that in CsI:Tl (0.06 mole %) at room temperature, STE formation amounts to $\leq 10\%$ of all electron-hole pairs created in a 662-keV electron track. It shows, furthermore, that the fraction of all initial excitations in the track that eventually result in STE capture at Tl^+ to form excited Tl^{+*} is $\leq 5\%$. This model result supports an extension to CsI:Tl at room temperature of the conclusion of Dietrich *et al.* [22] noted above, namely, that about 95% of the energy transfer to Tl is by binary electron and hole transfer, with STE transfer (reaction 4) only a small contributor (at perhaps 5%).

In summary, the detailed model results that we present below show that the two main factors favoring binary electron-hole energy transfer over STE transfer in Tl-doped alkali halides are the rapid spatial separation of hot electrons from self-trapped holes [24], combined with the very large capture rate of conduction electrons on Tl^+ [14,25]. The capture rate of electrons on Tl^+ (0.08%) is shown by picosecond absorption spectroscopy [25] to be even larger than the capture rate of electrons on self-trapped holes, so that doping CsI with approximately 0.08-mole % Tl (approximately equal to 0.3 wt % in melt) strongly inhibits STE formation. As a result of these findings, we will not consider reaction 4 involving STE energy transfer when seeking an explanation of the three main scintillation decay times in CsI:Tl.

A particular puzzle that we seek to answer in the rest of this section can be phrased as follows: Experiments have revealed three distinct decay components in CsI:Tl—730 ns, 3.1 μs, and 16 μs—but only reactions 2 and 3 are apparently available to account for them. Therefore, it seems that at least one of the two main reactions (2 or 3) must be contributing two distinct decay components of the scintillation pulse. How can that be? We look to plots of the time-dependent radial population and reaction rate from the model for insight.

B. Time-dependent radial population and reaction-rate plots

A good way to visualize the progress of various parts of the recombination process in the modeled track is to plot populations or reaction rates as a function of radius at a sequence of times for a given on-axis excitation density. Figures 6(a) and 6(b) plot the initial hole distribution along with Tl-trapped electron distributions (Tl^0) in the critical

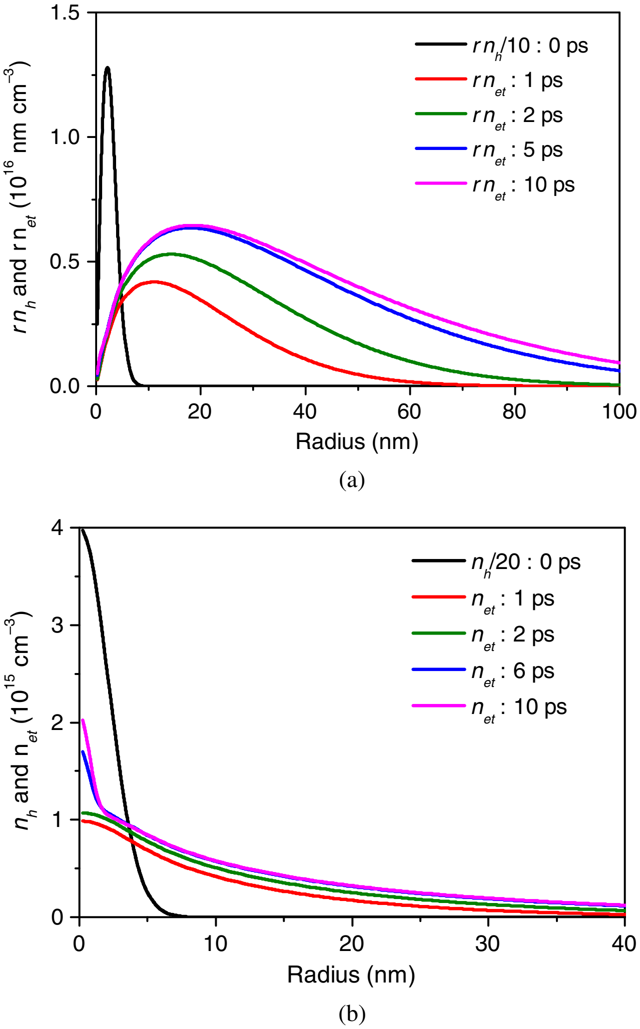

(a)

(b)

FIG. 6. The initial hole concentration profile, $[STH] = n_h$, is plotted, together with the thallium-trapped electron concentration, $[Tl^0] = n_{et}$, at early times up to the completion of electron trapping on Tl shortly after 5 ps. The on-axis excitation density is 10^{20} cm^{-3}. Two formats are presented. In (a), the population concentrations are multiplied by the radius to convey the number of carriers versus the radius. In (b), the concentrations are reported directly.

first 10 ps, when hot-electron diffusion drives the radial dispersal of electrons [24,37] that are trapped in picoseconds as Tl^0 (with a measured rate constant of $3 \times 10^{11}\ \mathrm{s}^{-1}$ for a 0.08-mole % Tl doping level [14,25]). This dispersal and trapping freezes in a charge-separated starting distribution of trapped electrons at larger radii of 40 nm or more and self-trapped holes close to the core in a radius of about 3 nm. As mentioned above, this electron-hole separation, together with electron trapping as Tl^0, discourages self-trapped exciton formation and is probably the main reason for the finding by Dietrich *et al.* [22] cited earlier that energy transport in Tl-activated KI and NaI occurs dominantly by binary electron and hole transport rather than STE transport. On longer time scales, as we see below, the STH diffuses outward and, ultimately, electrons thermally released from Tl^0 diffuse inward. In both cases, the carrier diffusion is assisted by the strong internal electric field set up by the early charge separation seen in Fig. 6, particularly at high excitation density.

In Fig. 6(a), the population concentration is multiplied by the radius to produce a result proportional to the number of carriers present at each radius. Because of hot-electron dispersal, the number of trapped electrons peaks at about 25 nm when thermalization and electron trapping on the Tl activator have ended. As described in Ref. [14], we set the hot-electron diffusion coefficient of the undoped CsI host in our model to reproduce the same radial distribution of electrons thermalized after 4 ps in CsI as were calculated by Wang *et al.* [24], a mean radius of about 50 nm, with some electrons dispersed as far as 200 nm. Upon including 0.08-mole % Tl in the modeled CsI with its measured electron-capture rate constant of about $3 \times 10^{11}\ \mathrm{s}^{-1}$ [25], the 25-nm mean radius of the Tl^0 population in Fig. 6(a) is found. Appreciable numbers of trapped electrons extend as far as 100 nm and beyond. The radially weighted plotting format of Fig. 6(a) was used in Ref. [14] with mixed units of $\mathrm{nm/cm}^3$, chosen so that division by the radius in nanometers recovers the local population density at that radius in cm^{-3}. Figure 6(b) simply plots the carrier concentrations versus radius. The reaction rates depend directly on the concentrations. We use both plotting formats as appropriate in the analysis and the discussions that follow. The narrow peaks at small radius in both frames of Fig. 6 are labeled as the initial hole population but represent the electron population equally well at $t = 0$. Their values are divided by the factors 10 and 20 in Figs. 6(a) and 6(b), respectively, to bring them on scale.

An immediate and striking conclusion to be drawn from Fig. 6(a) is that a great majority of the electrons are trapped within a few picoseconds on the Tl activator ions in CsI:Tl at radial locations that have little overlap with the self-trapped holes. The overlapped STH and Tl^0 populations inside a radius of about 6 nm are immediately subject to recombination, producing Tl^{+*} excited activators at a rate given by the term $B_{et} n_{et}(1 - f_e) n_h$ in Eq. (6). Following the terminology introduced in earlier studies [20,22,23,35], we call this process reaction 2. In the finite-element solution of our rate model, the local rate of $R2$ is nonzero only when there are overlapping populations of Tl^0 (local concentration n_{et}) and STH (concentration n_h) in the same cell. Thus, a significant portion of Tl^0-trapped electrons that do not spatially overlap the STH distribution in Fig. 6(a) cannot immediately contribute to the reaction-2 rate term. They become eligible if diffusion brings them into overlap. Such a diffusion is assisted by the internal electric field set up between the separated trapped charges.

To illustrate, Fig. 7 plots the time-dependent radial distributions of reaction 2 itself. The rate term that is responsible for reaction 2 is $B_{et} n_{et}(1 - f_e) n_h \approx B_{et} n_{et} n_h$, where n_{et} is the local density of Tl^0 (electrons trapped on the Tl^+ activator), n_h is the local density of the STH, and B_{et} is the bimolecular rate constant for this recombination of electrons and holes. The displayed results are calculated for an initial excitation density of $10^{20}\ e\text{-}h/\mathrm{cm}^3$ on axis of the track.

Figure 7(a) shows that, for roughly the first 200 ps, reaction 2 occurs only within a radius of about 6 nm where the STH and some of the Tl^0 overlap from the beginning. Starting around 1 ns, outward movement of the reaction zone tracking the diffusion of the STH to overlap additional Tl^0's at a longer radius can first be seen. The occurrence of significantly slower STH diffusion rates evaluated at lower excitation densities of 10^{19} and $10^{18}\ e\text{-}h/\mathrm{cm}^3$ (not plotted) demonstrates that Coulomb repulsion of the positive self-trapped holes in the track core significantly assists the STH transport outward. From about 4 ns onward, the outwardly advancing reaction zone leaves no significant activity in its wake because the Tl^0 population (at density n_{et}) is fully depleted by reaction with the dense advancing front of STH present at this excitation density and time range. Integrating the curve radially, we obtain the total $R2$ rate at each considered time. The quantity $n_{et} n_h$ proportional to the rate of $R2$ is plotted in Fig. 8 on a semilog scale. This curve is not a light decay one, but a plot proportional to the reaction-2 rate for creating Tl^{+*} excited states for an initial excitation density of $10^{20}\ \mathrm{cm}^{-3}$ on axis of the track. The $1/e$ time for decay of the main $R2$ rate is about 110 ns, corresponding to the straight line overlaid. Reaction 2 is itself a bimolecular recombination process. If the bimolecular rate term were the controlling factor in the decay at times longer than about 50 ns, we should expect a t^{-1} decay at long time periods rather than the exponential decay evident in Fig. 8. We regard the finding of first-order exponential-decay kinetics for this reaction at long time periods as partial evidence of transport-limited reactions of spatially separated populations at longer time periods.

The curve in Fig. 8 begins with a fast spike of about 1 ns duration. Considering the initial stationary reaction zone seen in Fig. 7, we conclude that the fast spike represents reaction 2 in the initially overlapping STH and Tl^0 populations, while the 110-ns decay component of the

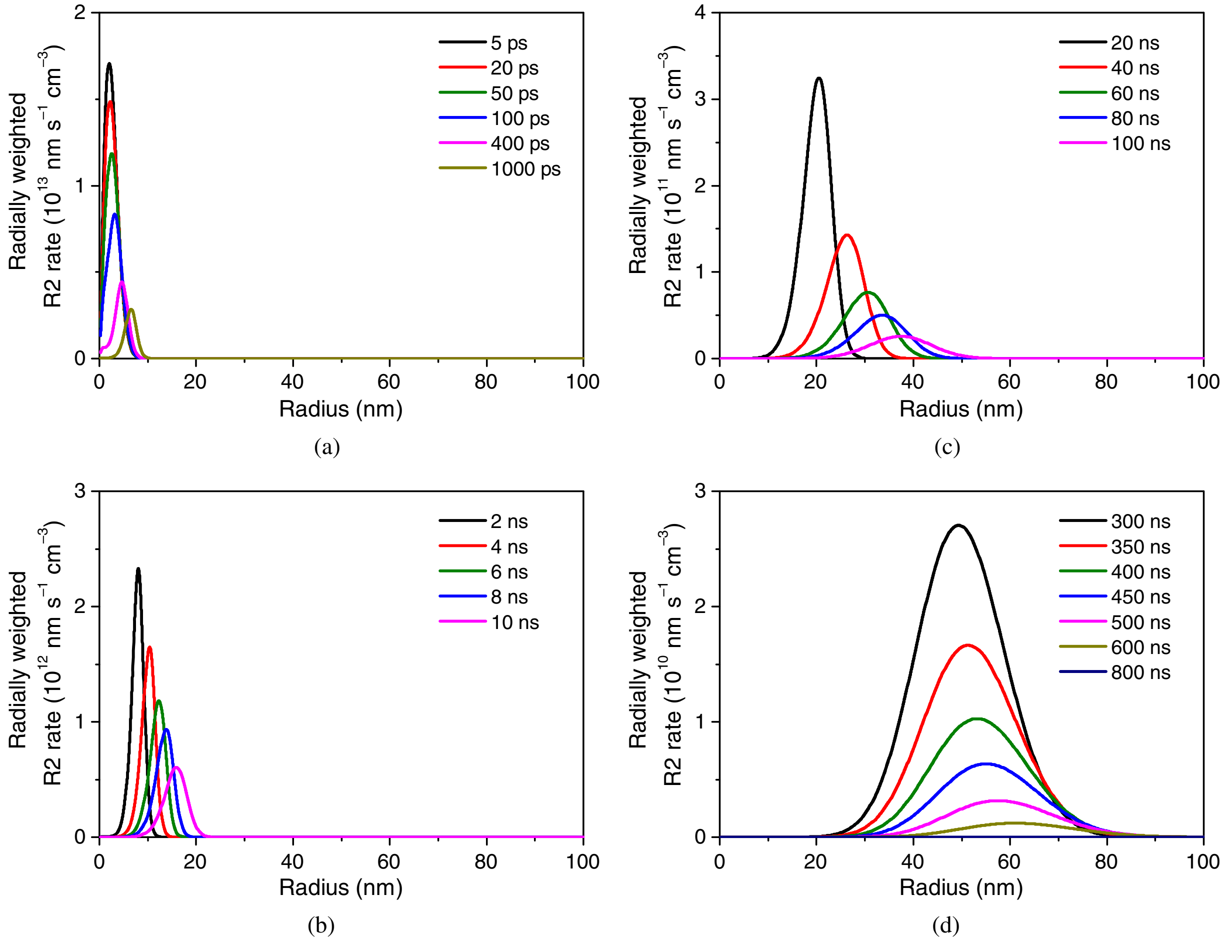

(a) (c)

(b) (d)

FIG. 7. The local rate of reaction 2 versus radius is plotted at evaluation times shown in the left two frames (a,b) from 5 ps up to 10 ns and continuing in the right two frames (c,d) from 20 to 800 ns. Reaction 2 ceases by 800 ns when the supply of STH is consumed by this reaction and by the competing process of STH capture on Tl^{+} activator sites to create Tl^{2+}.

main part of reaction 2 represents the transport-limited reaction rate of STH moving to encounter a new Tl^0 population. At the end of Fig. 7, reaction 2 can be seen taking place out to 80 nm, far beyond the initial zone of creation of STH, so STH diffusion out into the surrounding field of less mobile Tl^0's has obviously been important. The decay time of approximately 1 ns of the spike of reactions consuming the initial overlapped populations and the 110-ns decay of the STH transport-limited reaction rate are two different manifestations of a single reaction which we and previous writers have termed reaction 2 between STH and Tl^0.

Both the 1- and 110-ns decays for reaction 2 to form Tl^{+*} excited states are faster than the photoluminescence decay time of the excited Tl^{+*} state itself (575 ns), so the two components do not lead to observably different decay times of light emission, but rather contribute different rise-time components to the so-called fast scintillation component decaying with an approximately 730-ns time constant. The full-model calculation demonstrates in Fig. 2 that the formation rate of Tl^{+*} excited states with a time constant of about 110 ns, together with the 575-ns photoluminescence decay time of Tl^{+*}, provides a good match for the observed 730-ns decay time of the scintillation light. The prevailing view that reaction 2 is the main contributor to the 730-ns component is confirmed in this model, although we see later that reaction 3 also contributes a decay component

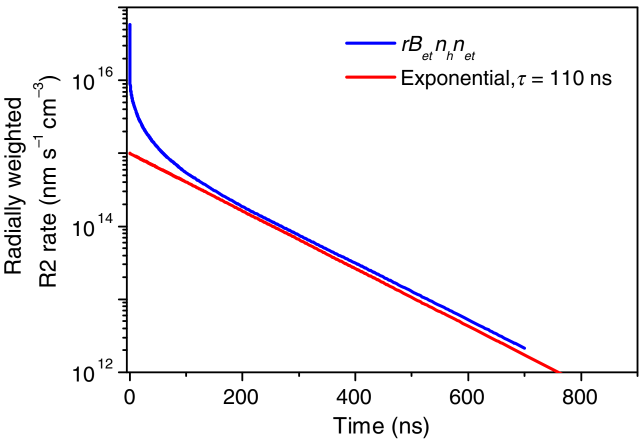

FIG. 8. Semilogarithmic plot of spatially integrated rate of reaction 2 versus time, for an on-axis excitation density of 10^{20} e-h/cm^3.

on the order of 800 ns. The model results in Figs. 7–9 confirm, furthermore, that reaction 2 expires too early (because of STH depletion) to be a contributor to either the 3- or the 16-μs scintillation decay component at the excitation density of 10^{20} e-h/cm^3 on axis that is illustrated here.

Figure 9 shows the radial population distributions of STH (rn_h), Tl^0 (rn_{et}), Tl^{2+} (rn_{ht}), and excited Tl^{+*} (rN_t) at six successive times, from 10 ns to 10 μs. The first population to take note of is STH. It can be seen on the radial axis that the STH population diffuses outward noticeably at times longer than about 10 ns. On the vertical axis, the number of STH can be seen decreasing rapidly with time in this early range as they encounter and combine with Tl^0 to produce Tl^{+*} excited states (reaction 2) and with Tl^+ to produce Tl^{2+}-trapped holes (setting up reaction 3).

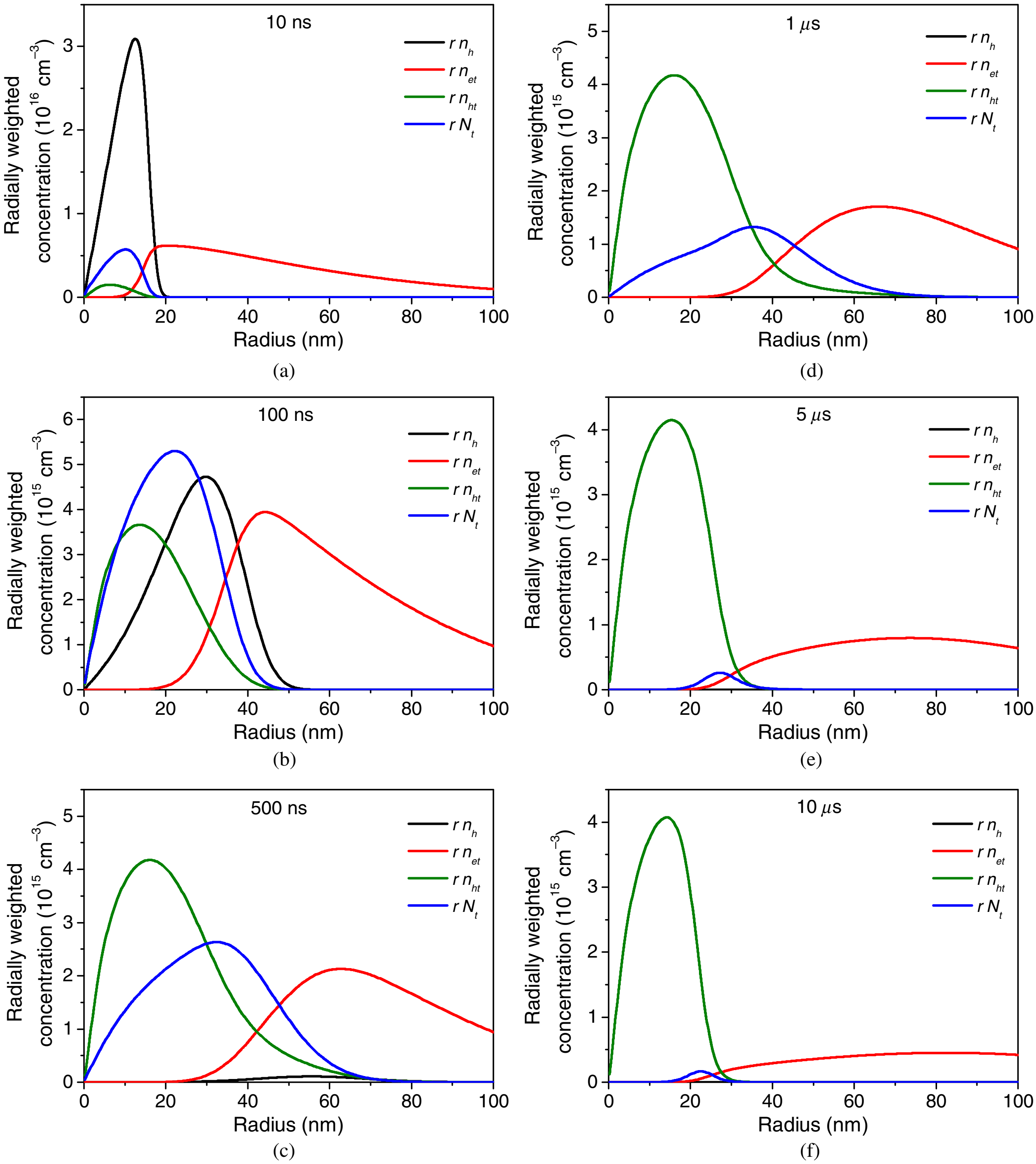

(a) (d)

(b) (e)

(c) (f)

FIG. 9. Plots proportional to azimuthally integrated local density of STH (rn_h), Tl^0-trapped electrons (rn_{et}), Tl^{2+}-trapped holes (rn_{ht}), and Tl^{+*}-trapped excitons rN_t are displayed as a function of the radius at six indicated times between 10 ns to 500 ns in the left column (a-c), continuing from 1 μs to 10 μs in the right column (d-f). The plots correspond to an on-axis excitation density of 10^{20} e-h/cm^3.

At 800 ns, virtually all STH have been consumed mainly by these two channels (i.e., n_h is written to zero when below 0.1% of its initial value shortly after 700 ns). At that point, $R2$ has effectively stopped.

As seen in the 500-ns frame of Fig. 9, most of the STH are exhausted by this time, but a population of Tl^{+*} excited activators (N_t) produced by $R2$ remain and are available for continued radiative decay. In addition, the partly overlapped, partly separated distributions of Tl^{2+} and Tl^0 that will produce subsequent additions to Tl^{+*} are evident. The overlapped Tl^{2+} and Tl^0 are immediately subject to recombination, producing Tl^{+*} at a rate given by the term $B_{tt}n_{et}f_e n_{ht}$ in Eq. (6), which we have termed reaction 3. A significant portion of Tl^0 trapped electrons that are not spatially overlapping the Tl^{2+} distribution in Fig. 9 cannot immediately contribute to this rate term for $R3$, but they become eligible if diffusion of electrons released from Tl^0 and recaptured elsewhere as another Tl^0 (assisted by the internal electric field of the separated charges that are clearly seen in Figs. 6 and 9) brings them into overlap. We have paraphrased the preceding two sentences from the discussion of $R2$ illustrated in Fig. 7 because the phenomena relating to reaction-rate- and transport-limited components apply in very analogous ways to both $R2$ and $R3$. In the case of $R3$, the rate- and transport-limited rates of creating excited Tl^{+*}'s are both slower than the Tl^{+*} radiative decay time, so it can be expected that both reaction rates of $R3$ may be observed as separate decay components of light emission.

Note that, particularly in the 0.5- and 1-μs frames of Fig. 9, the Tl^{2+} trapped-hole distribution develops a tail on its large-radius side extending unusually far into the Tl^0-trapped electron population. In fact, the Tl^{2+} tail extends all the way to the peak of the Tl^0 radial population distribution at about 65 nm. In the 5- and 10-μs frames of Fig. 9, the extended tail of Tl^{2+} has disappeared. This behavior suggests qualitatively that, in the time leading up to roughly 0.5 μs, STH diffusion and capture on Tl^+ creates a Tl^{2+} population overlapping Tl^0 population at a faster rate than reaction 3 could consume them. This oversupply results in storage of spatially overlapped reactant populations. The tail of Tl^{2+} population extending into the region with a high Tl^0 population seems to be one manifestation of that. After about 0.8 μs when STH are effectively exhausted, the overlapped populations of Tl^{2+} and Tl^0 should be the first consumed by $R3$ in the few-microsecond time range. We suggest that this explanation accounts for the 3-μs decay component of $R3$. When the main part of the stored-up overlapped reactant population is exhausted, as we might judge from the disappearance of the Tl^{2+} tail in the 5-μs frame, the subsequent decay of $R3$ is governed by the transport of released and recaptured Tl^0 electrons from their main population at large radius toward the reservoir of Tl^{2+} at a small radius. This transport-limited portion of $R3$ is suggested to be responsible for the 16-μs decay component. $R3$ is itself bimolecular, yet the 16-μs decay component is found experimentally (and in this model calculation as well) to be approximately exponential, signifying first-order kinetics. This result is consistent with its being a transport-limited reaction between spatially separated reactants. Notice the parallel reasoning between this discussion of the origin of the 3- and 16-μs decay components of $R3$ and the origin of the 1- and 100-ns rise components of $R2$. The difference is that $R3$ is slower than the 575-ns photoluminescence decay time of excited Tl^{+*}, while $R2$ is faster than that radiative time.

Recall that we ruled out reaction 4 (STE energy transport) as the source of any of the three main decay components because of the implications of extreme charge separation and electron trapping in Fig. 6. By elimination of the alternatives, attention is now focused on reaction 3 to understand from additional model perspectives how both the medium and tail decay components can arise from it.

Figures 10(a)–10(d) plot the radial dependence of the concentration of Tl^{+*} excited states resulting from all reactions calculated for on-axis excitation density of 10^{20} cm^{-3}, sampled at times from 5 ps to 10 μs, as labeled in the legends. The time sequence increases going down the left column and then going down the right column, ending at 20 μs. Notice that the radial-scale range and the vertical-axis range both change as time goes on. For the first 100 ps, the Tl^{+*} excited states are formed at an increasing rate "in place" defined by the initial STH distribution overlapping that part of the Tl^0 population formed near the axis. The total number of excited states (integrated azimuthally and radially) is small in this stage. At times longer than about 200 ps, a shoulder progressing out to a larger radius indicates the onset of significant STH diffusion, resulting in overlap with additional Tl^0's to sustain reaction 2. This diffusion continues out to 800 ns in Fig. 10(c), at which time the supply of STH is exhausted, as we see in Figs. 7 and 9. By this time, an underlying contribution from reaction 3 has developed, so Tl^{+*} formation is maintained going forward beyond 800 ns.

These plots of Tl^{+*} at various times give additional clues to the origin of the two distinct decay times found in a range longer than 730 ns, where reaction 3 is the only substantial recombination reaction still taking place. Indeed, the last frame in Fig. 10 showing times from 1.5 to 20 μs displays a distinct change in height, width, and shift of radial position versus time for the peak in the Tl-trapped exciton population, starting after 3 μs.

The dominant radial distribution for times from 1.5 to 3 μs is a peak in Tl^{+*} fixed at about 36 nm, overlying a background that slopes downward with an increasing radius. The background falls away due to Tl^{+*} radiative decay over the interval from 0.8 to 1.5 μs, revealing the stationary peak at 36 nm quite clearly as a main contributor to the rate of Tl excited-state production during this few-microsecond range. Considering the 575-ns decay time of

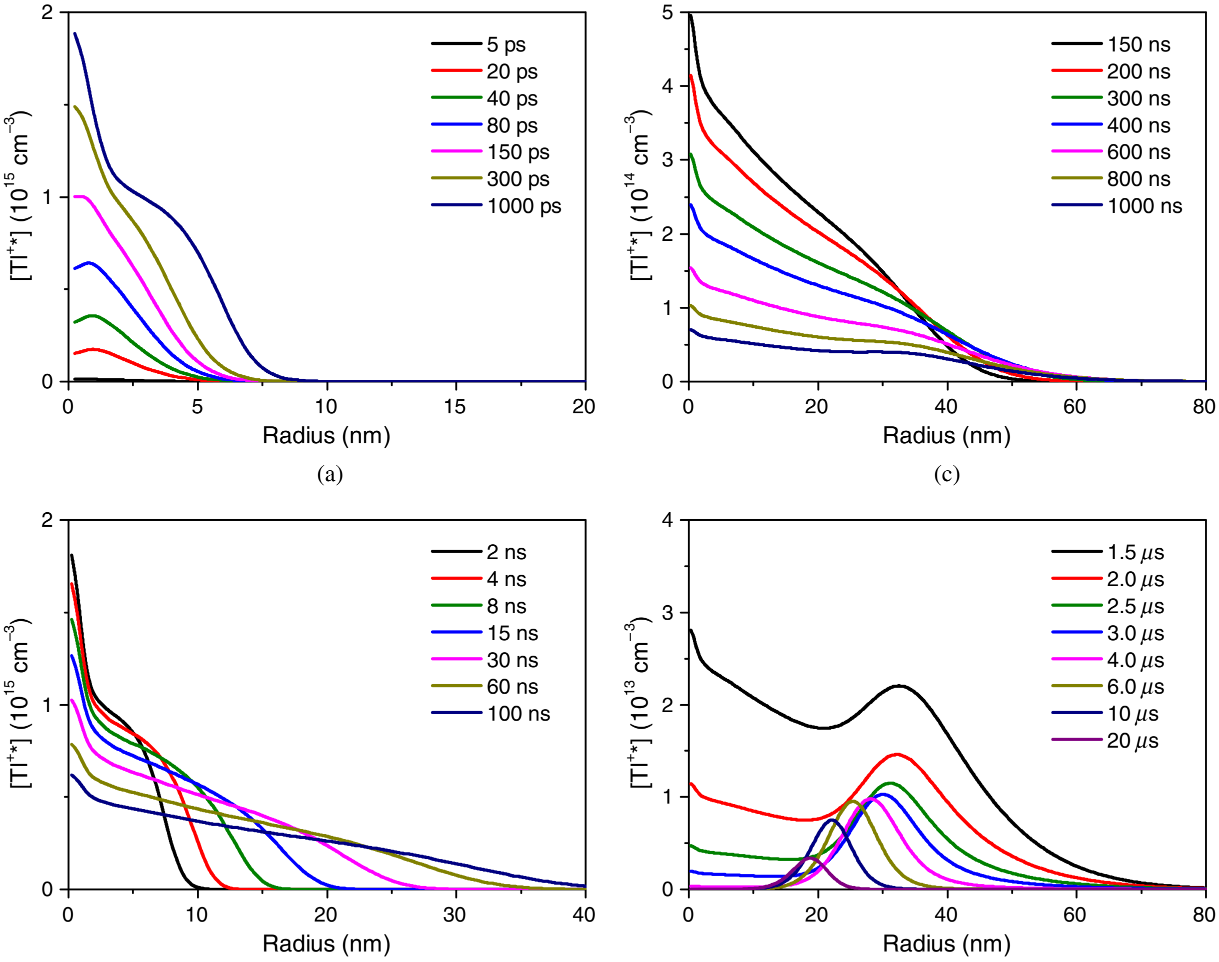

(a) (c) (b) (d)

FIG. 10. The Tl^{+*} excited state (N_t) concentration distribution resulting from all reactions at an on-axis excitation density of 10^{20} cm^{-3} is plotted versus radius at times sampled from 5 ps to 100 ns down the left column (a,b) and 150 ns to 20 μs down the right column (c,d). Notice that the radial-scale range and the vertical-axis range both change as time goes on.

Tl^{+*}, the time interval of dominance of this 36-nm peak in the radial distribution of the reaction-3 production of Tl^{+*} lines up with the experimental 3-μs decay component of light emission. Recall that, in Fig. 9, we can see a tail of the Tl^{2+} distribution penetrating deep into the Tl^0 population during the few-microsecond period, suggesting that overlapped reactants are being stored in the radial range from 30 to 60 nm during the first 0.5 μs, and that afterward they are being consumed by $R3$. We may conclude that the peak of the radial reaction zone producing Tl^{+*} in Fig. 10 from roughly 1 to 3 μs remains stationary because it is running mainly on the overlapped populations that were stored previously. When those stored overlapped populations are exhausted, the $R3$ reaction zone begins to shift inward toward a small radius, as the continued $R3$ depends on diffusion of the electrons untrapped from Tl^0 to find Tl^{2+} at smaller radius.

Starting at about 3 μs in Fig. 10(d), the formerly stationary radial peak in the Tl^{+*} population shifts toward a smaller radius, as just noted. It assumes a smaller width and a gradually decreasing height out to 20 μs. Empirically, it seems natural to associate this radially shifting and slowly decreasing zone of $R3$ with the 16-μs decay component. This deduction strongly suggests that the 3- and 16-μs decay components both come from $R3$ (thermally ionized Tl^0 electrons reacting with stored Tl^{2+} trapped holes), with the distinct decay times rooted in different spatial distributions of the reactants, calling into temporary dominance different rate terms in Eqs. (4)–(6).

When the transport arrival rate of carriers increases the product of reactants faster than the bimolecular reaction rate governed by $B_{tt}^0 n_{ht} n_{et} f_e$ can decrease it, the $R3$ rate producing Tl^{+*} is not transport limited. Also, if the product of local reactant densities built up from previous trapping added to the transport into that location supports a bimolecular recombination rate faster than the arrival of new overlapped populations, once again, the $R3$ rate producing Tl^{+*} is not transport limited. The rate in these cases will be set by the bimolecular rate constant B_{tt}^0 multiplying the local product of densities in place. As time goes on, the bimolecular rate of in-place reactions will consume the stored excess population of the overlapped carriers. We propose that such an in-place reaction combined with radiative decay is happening in Fig. 10(d) between about 1.5 and 3 μs. The bimolecular rate falls until it equals the rate of increase of the reactant density product due to the transport processes (1) and (2) listed above. When the reaction rate becomes equal to the transport rate, the rate of the bimolecular reaction is transport limited and should be determined partly by the concentration gradient and the electric field that drive directional transport. By contrast, the rate term $B_{tt}^0 n_{ht} n_{et} f_e$ for bimolecular recombination does not depend directly on concentration gradients or electric fields. In this way, two distinct decay components of $R3$ can arise.

Figure 2, showing calculated light emission as a function of time, confirms that the rates of Tl^{+*} production which are dissected in Fig. 10 do indeed produce scintillation decay times corresponding to the observed values of 730 ns, 3.1 μs, and 16 μs. We conclude again that the latter two are due, respectively, to the non-transport-limited and the transport-limited bimolecular reaction 3 between Tl^{2+} and Tl^0.

Figures 11–13 below provide further support for this conclusion. Figure 11 illustrates the transition from an in-place consumption of local stored densities of reactants to a transport-limited reaction at a slower rate. The radially weighted rate of change of local density of Tl^0 due only to transport is plotted with solid curves, while the radially weighted rate of change of local density of Tl^{2+} at corresponding times is plotted with dashed curves. The latter are fully negative because production of any new Tl^{2+}'s ceases shortly after 700 ns, the first curve shown in this figure. Tl^{2+} are assumed not to diffuse on time scales of interest in scintillation, so the reason for their population to decrease in this model is $R3$, in which a Tl^{2+} and a Tl^0 are annihilated as a pair with production of Tl^{+*}. Thus, the dashed curves also represent an identical loss of Tl^0 by $R3$ recombination. In these terms, Fig. 11 may be considered to compare radially weighted profiles of rate of change of $[\mathrm{Tl}^0]$ due to reaction 3 occurring in place (recombination, dashed

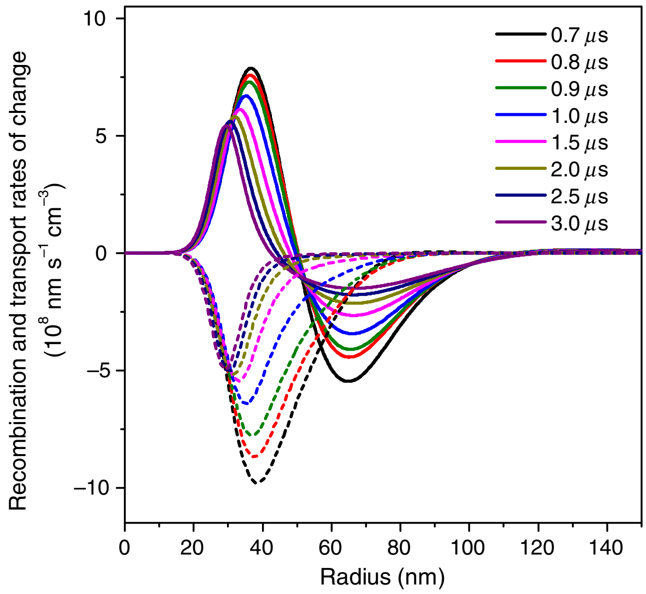

FIG. 11. Radially weighted profiles of rate of change of $[\mathrm{Tl}^0]$ due to reaction 3 occurring in place (recombination, dashed curves) and due only to transport by diffusion and electric current (transport, solid curves) are compared at the indicated times. After about 3 μs, the rate of loss of $[\mathrm{Tl}^0]$ due to recombination with $[\mathrm{Tl}^{2+}]$ approaches equality with the positive gain of $[\mathrm{Tl}^0]$ due to transport. This approach to equality marks the onset of the transport-limited regime.

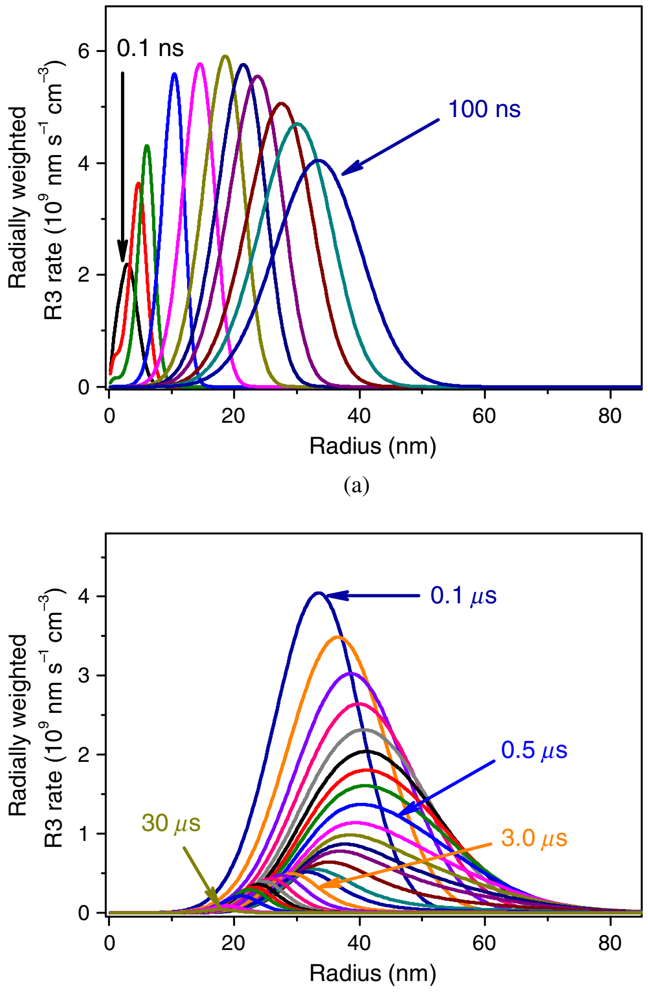

(a)

(b)

FIG. 12. Radially weighted profiles of the $R3$ reaction rate are plotted for the times (a) 0.1, 0.5, 1, 5, 10, 20, 30, 40, 60, 80, and 100 ns, and (b) 0.1, 0.15, 0.2, 0.25, 0.3, 0.35, 0.4, 0.45, 0.5, 0.6, 0.7, 0.8, 0.9, 1, 1.5, 2, 3, 4, 5, 6, 7, 8, 9, 10, 20, and 30 μs. The radial weighting factor r comes from azimuthal integration of the cylindrical track to assess the total reaction rate versus the radius. Mixed units of 10^9 nm s^{-1} cm^{-3} are used as in Ref. [14], so division by the radius in nanometers recovers the local reaction rate at that radius in units of s^{-1} cm^{-3}.

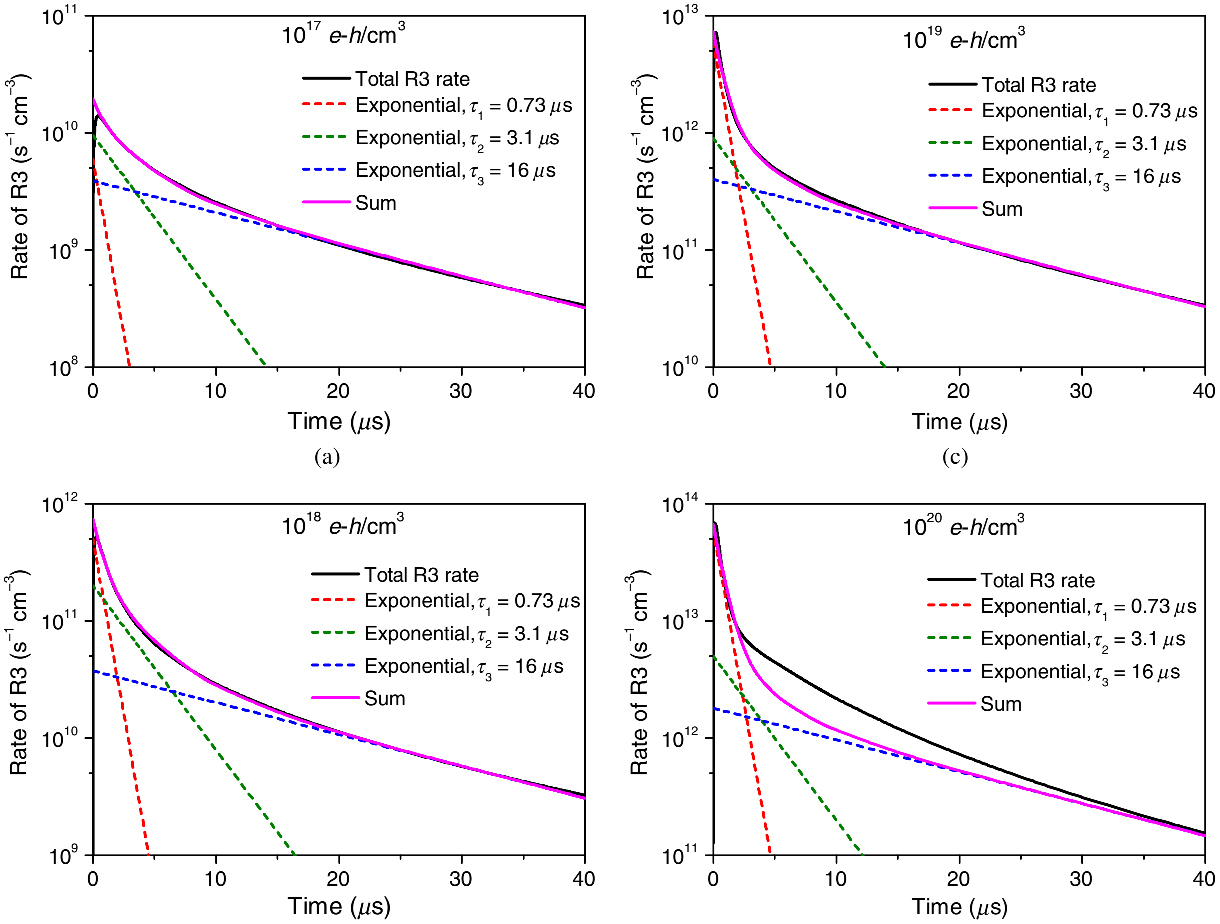

(a) (c)

(b) (d)

FIG. 13. The spatially integrated rate of reaction 3 (the black curve) is plotted as a function of time on a semilog scale for excitation densities of (a) 10^{17}, (b) 10^{18}, (c) 10^{19}, and (d) 10^{20} e-h/cm^3. This model result represents the time-dependent rate of change of the number of Tl^{+*} excited activators due solely to $R3$. It is the main contributor to the Tl^{+*}-emitting state population at times longer than 700 ns. Three exponential-decay components—730 ns, 3.1 μs, and 16 μs—found to characterize the 662-keV scintillation decay [12] are fitted and displayed along with their sum in the magenta curve, which can be compared to the model-calculated black curve.

curves) and due only to transport by diffusion and electric current (transport, solid curves) at the indicated times.

When the transport-limited regime is attained, every Tl^0 arriving in the reaction zone by diffusion and electric-current transport of the thermally released electron should correspond pairwise to the loss of a Tl^{2+} from the reaction zone. The positive peak of the Tl^0 transport curve should come to have the same height, width, and radial position as the inverted peak of the Tl^0 and Tl^{2+} pairwise consumption curve. It can be seen in Fig. 11 that this consequence occurs for times of approximately 3 μs and greater. At earlier times, the dashed curve exceeds the transport peak of Tl^0 arrivals in height and width, consistent with the consumption of locally stored Tl^{2+} and Tl^0 populations to feed part of the bimolecular recombination via reaction 3 during the (1–3)-μs interval of the middle decay component.

Figure 12 presents a time sequence from 100 ps through 30 μs for the $R3$ rate term $B_{tt}^0 n_{ht} n_{et} f_e$, where n_{ht} is the Tl^{2+} density, $n_{et} f_e$ is the local density of Tl^0's that are thermally ionized in equilibrium, and B_{tt}^0 is the bimolecular rate constant for reaction 3.

Figure 12 confirms much of what was seen in earlier radial representations of different data, particularly Fig. 10. The rate of $R3$ increases rapidly at a small radius over approximately the first 1000 ps. In the overview of the earlier times in Fig. 12(a), we can see that the reaction rate for $R3$ initially grows versus time, inside a 10-nm radius, for about the first 1000 ps. Since the density profile for Tl^0-trapped electrons, n_{et}, is established in the first 10 ps, the growth in height of this $B_{tt}^0 n_{ht} n_{et} f_e$ reaction peak is due to an increase of n_{ht}, the density of Tl^{2+}, by capture of STH from the intense peak at the small radius seen in Fig. 6(a). This process is governed by the rate term $S_{1h} n_h$ appearing in Eq. (2) as a loss and in Eq. (5) as a source term. The evolution from about 10 ns to 0.5 μs is mainly that of a radially translating reaction zone tracking the STH diffusion front as it creates a new Tl^{2+} population overlapping an existing Tl^0 population.

From 0.5 to about 3 μs, the width of the zone decreases rapidly as its peak shifts inward toward a smaller radius. This narrowing coincides in time with the previously noted evidence for consumption of the stored overlapping Tl^{2+} and Tl^0 populations around a (40–60)-nm radius that are accumulated faster than the $R3$ reaction could occur in the preceding 0.5 μs. Thereafter, until the last plot at 30 μs, a narrow reaction zone moves inward as a transport-limited reaction fueled by the arrival of Tl^0 (diffusion by electron release and recapture) from the reservoir at larger radius. This sequence is the same one that is evident in Fig. 10, told this time from the perspective of the $R3$ rate term.

The profile of $R3$ represented in Fig. 12 is integrated over the radial coordinate to obtain the total reaction-3 rate as a function of time. The resulting time dependence of the $R3$ rate is plotted in Fig. 13(d) for the excitation density 10^{20} $e\text{-}h/\mathrm{cm}^3$ on axis, the same value used for the illustrations in Figs. 6–12. In Fig. 13, we also show results for 10^{17}, 10^{18}, and 10^{19} $e\text{-}h/\mathrm{cm}^3$ on axis and, in all of the frames, we have attempted to reconstruct the decay curve in terms of the three exponential-decay times, 730 ns, 3.1 μs, and 16 μs, found to fit the experimental scintillation decay data (662 keV) [12]. As shown earlier, reaction 2 ($\mathrm{STH} + \mathrm{Tl}^0 \rightarrow \mathrm{Tl}^{+*}$) is mainly responsible for the 730-ns scintillation decay, and that reaction is not represented in Fig. 13. Nevertheless, $R3$ turns out to exhibit a fast component of the reaction-rate decay in the range of 700 ns as well, so the 730-ns decay time is included in the analysis. The main interest driving this analysis is in the 3.1- and 16-μs components of $R3$. We have seen that $R2$ goes to completion within 800 ns at 10^{20} $e\text{-}h/\mathrm{cm}^3$ and 1.4 μs at 10^{17} $e\text{-}h/\mathrm{cm}^3$, so the two longer decay components of scintillation should arise mainly from $R3$. Furthermore, since these longer decay times significantly exceed the 575-ns photoluminescence decay time of Tl^{+*}, the longer components of scintillation decay can be expected to track the decay of the total $R3$ reaction rate producing Tl^{+*}.

The three-component analysis in Fig. 13 shows reasonably good fits at 10^{17}, 10^{18}, and 10^{19} $e\text{-}h/\mathrm{cm}^3$, but a substantial under-representation at 10^{20} $e\text{-}h/\mathrm{cm}^3$ from about 5 to 30 μs. This analysis serves as a reminder that the scintillation is a weighted sum over many contributing local excitation densities. Furthermore, the analysis indicates a reduction of the 730-ns component as the excitation density is lowered, trending toward a mostly two-component sum of 3.1- and 16-μs decay for the $R3$ curve at 10^{17} $e\text{-}h/\mathrm{cm}^3$.

The collective effect of all of the excitation densities to $R3$ can be calculated by weighting each according to its frequency of occurrence in a 662-keV electron deposition using GEANT4. This procedure is analogous to the method for weighting the local light yield in our full scintillation model. The result for the weighted $R3$ is shown in Fig. 14. The model-calculated $R3$ decay curve in blue is matched fairly well by the sum of 730-ns, 3.1-μs, and 16-μs components in orange. Two small discrepancies around 4 and 16 μs remain and are similar to the full-model fits of scintillation decay in Fig. 2. If the 3.1-μs decay time is replaced by a 4-μs decay time, a nearly exact match with the calculated $R3$ curve is obtained, but we will stay with the set of fixed decay times from the experimental study [12].

We regard Fig. 14 as confirmation that the $R3$ reaction rate for the weighted sum of excitation densities in a 662-keV track can be well represented by the three decay-time components of scintillation [12], even though that representation fails, to some degree, at high excitation densities around 10^{20} $e\text{-}h/\mathrm{cm}^3$. Two notable features emerge at 10^{20} $e\text{-}h/\mathrm{cm}^3$ in Fig. 13(d). The 3.1-μs component has yielded strength to a 730-ns component in the fitting at high density. Effectively, what is the faster (approximately 3 μs) of the two main slow components of $R3$ at lower excitation densities becomes faster still at high density and contributes light in the same general time range as the main, 730-ns fast component of scintillation due to $R2$. In experimental observations of scintillation pulse shape versus gamma energy, this contribution appears as an increase in the ratio of fast compared to slow and tail components at low gamma energy, i.e., high excitation density. This appearance is the observed experimental trend. Part of the reason is identified with an increasing contribution of $R3$ in the same time range as the fast component of mainly $R2$ light emission. Other reasons for this energy dependence of pulse shape

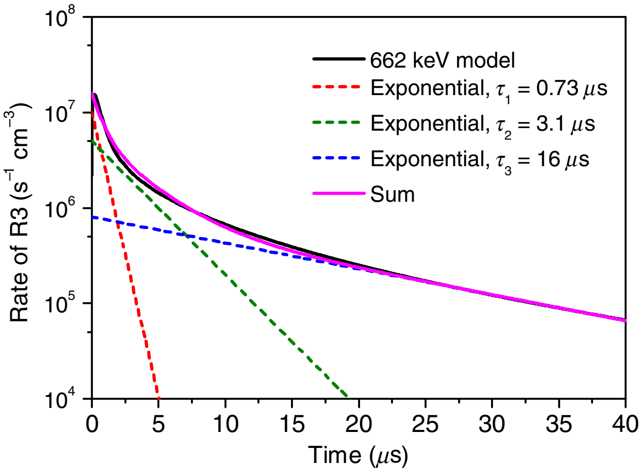

FIG. 14. The rate of reaction 3 as a function of excitation density is weighted by the probability of occurrence of each excitation density in a 662-keV electron track based on GEANT4 simulations and is displayed versus time in the black curve. Three exponential-decay components—730 ns, 3.1 μs, and 16 μs—found to characterize a 662-keV scintillation decay [12] are fitted and displayed along with their sum in the magenta curve, which can be compared to the model-calculated black curve.

can be found in the kinetics and spatial dependence of $R2$ itself, as already discussed.

In addition, Fig. 13 shows that the tail decay time trends to a shorter value than 16 μs at the higher excitation densities, especially 10^{20} e-h/cm^3. The experimental trend found in Ref. [12] was that, at low gamma energy, the tail decay time becomes slightly faster, e.g., 14 ± 3 μs at 6 keV.

Figure 13 shows that the empirical "3-μs decay time" is not a single identified process with that decay time, but rather the weighted sum of multiple decay times dependent on excitation density that vary through the roughly $(10 - 0.7)$-μs range, as excitation density encountered in a track spans the corresponding densities. This observation leads us, finally, to reconsider whether the characterization of the scintillation decay by three exponential components need imply that the light is coming from rigorous "exponential-decay processes," i.e., pure first-order decay. It does not. The fast and slow components are demonstrably not rigorous exponential functions. Although this model provides justification for why the transport-limited tail component would obey an approximately first-order decay law, exact first-order decay would not result given the complexity of the tracks, and the data themselves are, frankly, too noisy to assert exact exponential decay in the tail. Whether multiexponential or nonexponential with identified fast, slow, and tail components near 0.73, 3.1, and 16 μs, these data are the ones modeled.

VI. ORIGIN OF ANTICORRELATED FAST AND TAIL PROPORTIONALITY TRENDS AT ROOM TEMPERATURE

As can be seen in Fig. 5, the model predicts proportionality curves of the fast and tail components of scintillation showing the same remarkable anticorrelation of trends for these two components as was found in an experiment [12]. The measured fast component falls as energy increases from 16 to 662 keV, while the tail component rises over the same increasing energy interval. To get at the physical mechanisms behind this anticorrelated behavior of fast and tail proportionality curves, we make use of the results in the previous section confirming that the fast decay component (730 ns) is mainly due to reaction 2, and the tail component (16 μs) is due to the transport-limited part of reaction 3. As has been discussed, the rate term in Eq. (6) that is responsible for reaction 2 is $B_{et} n_{et} (1 - f_e) n_h$, and the rate term responsible for reaction 3 is $B^0_{tt} n_{et} f_e n_{ht}$. These rate terms are not light outputs, but they both feed the Tl^{+*} population from which light is emitted.

In Fig. 15, the excitation-density dependences of the yields of $R2$ and $R3$ producing Tl^{+*} excited states are plotted in blue and red, respectively. We could call this plot the "local yield of reactions 2 and 3" in analogy to what we have previously called local light yield as a function of excitation density. The dashed black curve and the gray horizontal line labeled "Murray-Meyer" are discussed later.

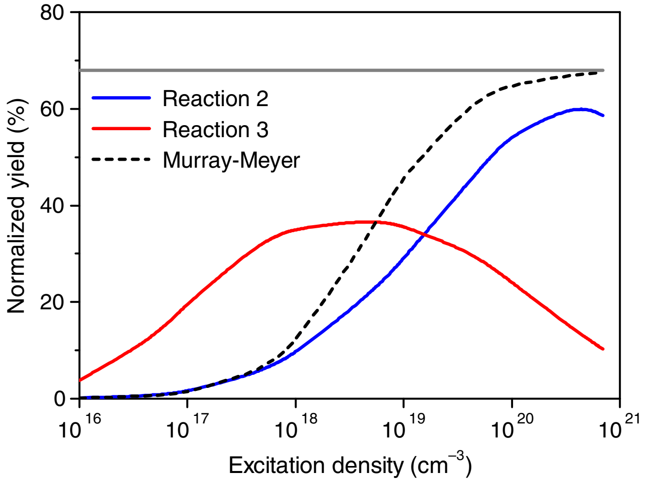

FIG. 15. The time- and space-integrated yields of reactions 2 and 3 are plotted versus initial on-axis excitation density with the solid blue and red curves, respectively. The yield is integrated from zero to 40 μs.

Look first at the blue solid curve for the yield of reaction 2. It starts near zero at a very low excitation density and rises with a concave upward curvature, consistent with the fact that reaction 2 is bimolecular in populations whose initial values scale roughly with excitation density. We say "roughly" because it should be apparent from the above discussion and radial plots that the product of overlapping STH and Tl^0 densities varies dramatically in time and space as a result of hot-electron diffusion in the beginning followed by electric-field-driven diffusion reuniting free carriers and trapped carriers over time. In sweeping terms, however, the supply of reactant populations that can participate in transport and recombination is roughly proportional to the initial excitation density, so we should not be surprised that the $R2$ yield (i.e., the blue curve) looks similar to the dashed curve (discussed below), which is a bimolecular yield competing with a linear loss in a limited population. Above about 7×10^{19} e-h/cm^3, the blue curve starts to bend over and eventually turns downward. This trend is understandable, first because the supply of reacting carriers is limited, so it must be a saturating yield that finally bends toward a finite value if there are no losses. The limit of the saturating yield is lowered by second-order quenching and the sharp turndown above 4×10^{20} e-h/cm^3 can be attributed to third-order Auger quenching.

Bearing in mind that Fig. 15 plots the local reaction yield as a function of excitation density, not the light yield as a function of gamma energy, one nevertheless can see that the fast reaction-2 curve has a shape consistent with the proportionality curve of the fast 730-ns scintillation component shown in the experimental results of Fig. 5(a). In making this comparison, we qualitatively associate high gamma energy with predominantly low excitation density and low gamma energy with predominantly high excitation density.

Now focus on the solid red curve plotting the local yield of the slower $R3$. For excitation densities above 10^{18} $e\text{-}h/\text{cm}^3$ that comprise most of the energy deposition in high-energy electron tracks, the curve of the $R3$ yield is flat or turns downward with increasing excitation density. This trend is anticorrelated with the increasing yield of $R2$ versus excitation density, just as seen in the experimental fast and tail proportionality versus gamma energy [Fig. 5(a)]. The essential reason for this anticorrelation is quite basic; namely, the two processes compete for the same STH supply in two different kinetic orders. Reaction 2 ($\text{STH} + \text{Tl}^0 \rightarrow \text{Tl}^{+*}$) is bimolecular in excitation products and, therefore, wins at high excitation density over the first-order process of Tl^{2+} formation ($\text{STH} + \text{Tl}^+ \rightarrow \text{Tl}^{2+}$). The latter process obeys first-order kinetics because Tl^+ is a crystal dopant, not an excitation product. Since Tl^{2+} is a reactant for $R3$, we see the result of the competition as a decrease in $R3$ at high density in Fig. 15. The reaction-3 rate term is proportional to the product of two trapped-carrier populations, both of which are essentially the "leftovers" after completion of the faster reaction 2. By about 3 μs, when we can first clearly identify the tail component, $R2$ has run to completion and has consumed 54% of the starting STH and Tl^0's at 10^{20} $e\text{-}h/\text{cm}^3$, versus 9.5% of the starting STH and Tl^0's at 10^{18} $e\text{-}h/\text{cm}^3$, according to the model results. Most of the STH not used in $R2$ are converted by capture into Tl^{2+} and serve as one reactant for $R3$. Most of the Tl^0's not used in $R2$ will be used as the other reactant in $R3$. The yield of reaction 3 scales approximately as the product of two nearly equal populations that are both leftovers after the completion of reaction 2. In those general terms, the yield of $R3$ in this system must be anticorrelated with the yield of $R2$ versus the excitation density and, therefore, versus gamma or electron energy in the reversed sense of how particle energy and effective excitation density are approximately related. The anticorrelation displayed in the experimental measurements of Fig. 5(a) is a direct consequence. The ratio of carriers being used in $R2$ or left over for $R3$ is influenced by the electric-field-assisted transport of STH in the first phase, which is dependent on the excitation density.

Reaction 3 is itself bimolecular since the Tl^{2+} and Tl^0 reactants [in the sense of the corresponding rate term in Eq. (6)] are both excitation products. This characteristic accounts for the rising slope of $R3$ with excitation density at low densities in Fig. 15, i.e., before $R2$ begins to deplete the STH supply in second order faster than the first-order $\text{STH} + \text{Tl}^+$ capture can use them. The fact that $R3$ starts out larger than $R2$ at low carrier densities is also understandable because a large fraction of STH are converted to Tl^{2+}'s at low excitation density, where first-order capture on numerous activators competes well with bimolecular recombination.

Proceeding from reaction yields versus excitation density to reaction yields versus electron energy, Fig. 16 plots the result of weighting the reaction yields at various densities in Fig. 15 by the probability of each density occurring in the GEANT4 simulations for a given initial electron energy. Repeating the procedure for various electron energies produces the curves in Fig. 16, giving the reaction yield ($R2$ or $R3$) for that initial energy. Note that the energy dependences of the yields for $R2$ and $R3$ have the same general form as the proportionality curves of fast and tail decay components in Fig. 5.

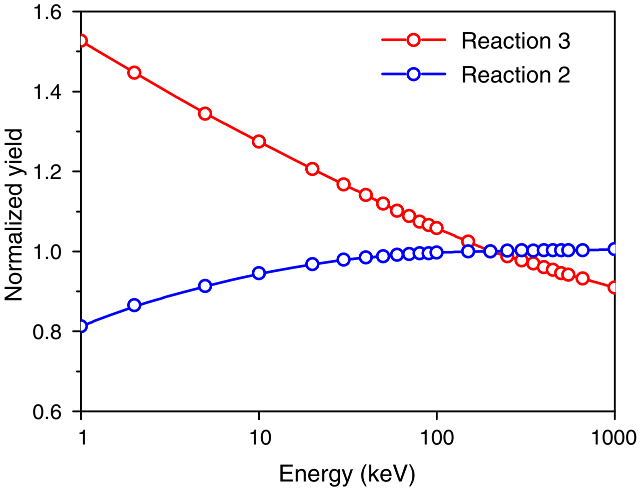

FIG. 16. The yields of reactions 2 and 3 evaluated after 40 μs are plotted versus the initial electron energy.

Before leaving this topic, it is worthwhile to try to connect the results with the approximate treatment by Murray and Meyer of competing bimolecular exciton formation and defect trapping in a line track [35]. They postulated a system in which the free electrons and holes are created pairwise in linear number density $n = n_h = n_e$ along a line of deposition. They considered "… that the electron can suffer two events, either recombining with a hole in the wake of the incident particle, or trapping at an unspecified site in the lattice," the latter according to a first-order trapping rate Kn. The productive bimolecular rate of electron-hole recombination to form the excitons that they suggested are responsible for Tl^{+*} emission can be written as the second-order term Bn^2. The productive rate divided by the sum of all rates defines a yield written as

$$Y = \frac{Bn^2}{Kn + Bn^2} = \frac{\alpha n}{1 + \alpha n}, \tag{9}$$

where $\alpha = B/K$. The expression on the right-hand side of this equation is the Murray-Meyer statement of the expected radiative yield in this system. This expression describes a yield decreasing as the excitation number n decreases (in an assumed line deposition). The expression starts from near zero at a small n, rises quadratically at first, and approaches a saturating constant value of unity at a large n. It does not turn down at large n's, but it saturates at unity because Murray and Meyer did not include either second-order (dipole-dipole) or third-order

(Auger) nonlinear quenching. Equation (9) is plotted in Fig. 15 with the dashed black curve, and its saturation asymptote with a solid gray line.

As noted above (and also by Murray and Meyer [35]), this simple formula can give only a qualitative illustration of what goes on in a real particle track. As we see in Fig. 6 and the surrounding discussion, roughly 90% of the electrons and holes are separated by hot electron diffusion and are trapped or self-trapped in different radial zones early in the pulse evolution [14,37]. There are important electric-field effects and trapping at play in their eventual recombination. As we have already noted, there are also nonlinear quenching terms not included in the Murray-Meyer formula. A solution of the full-model description of transport, trapping, and recombination is necessary to make quantitative predictions of the light yield versus the particle energy, i.e., results such as those shown in Fig. 5(b). Nevertheless, a comparison of the Murray-Meyer curve and the reaction-2 curve in Fig. 15 reveals considerable similarity. This similarity confirms that, fundamentally, reaction 2 is bimolecular in excitation density when sufficient time is allowed for transport and recombination of dispersed trapped-carrier populations. The main linear trapping channel that competes with $R2$ in the Murray-Meyer sense is actually STH capture on Tl^{+} to make Tl^{2+}. Although this trapped-hole species will later produce light in $R3$, it is a dark defect trap with respect to the fast scintillation of $R2$. Electron trapping on deep defects in this model is also a competitor with $R2$, but on a smaller scale than linear hole trapping to form Tl^{2+}, simply because the concentration of the Tl^{+} dopant exceeds the defect concentration in most cases.

VII. THE MATERIAL INPUT PARAMETERS

As described in Ref. [14], the model of scintillation that we have constructed tries to take into account the important physical processes of carrier generation, transport, recombination, nonlinear quenching, and capture on dopants and defects that seem logically required for a physical description of the events in a particle track from which light yield and proportionality are determined. The number of material parameters necessary to specify those terms in a system of equations for free and trapped electrons, holes, and excitons is large, as was enumerated in Tables I and III of Ref. [14] for undoped and Tl-doped CsI. The good news about this circumstance is that for a model to yield information about effects caused by variation of material composition (concentration and species of doping, codoping, defects, etc.), the coefficients and rate constants of all of those components should be in the model, or no specific information on material engineering by their variation can be obtained. The bad news is that good values for all of the parameters must be supplied whenever a new material system is modeled. Thus, there is a time investment for each new material. Over time, a library of tested parameter sets for important scintillator systems of interest should be built up. We believe that the material input parameters for CsI and CsI:Tl are approaching a reasonably well-tested status by virtue of the fitting and predictions of pulse shapes, energy dependence, absolute light yield, and proportionality (both in total and by decay component) in this work, evolving from the initial set in Ref. [14]. Undoubtedly, there will be some further refinement of the material parameter values following direct experimental measurements and theoretical work in the future. Over time, however, validated parameter sets for a number of important scintillator systems should emerge from continuing work on CsI:Tl, and then on other materials as well.

Table I lists the parameters of CsI, all of which except for the deep defect-trapping rate constant K_{1e} remain unchanged in this work relative to the values used for the calculation of proportionality and light yield in undoped CsI at 295 K in Ref. [14]. Note that the material parameters of undoped CsI are also used to describe the host when modeling CsI:Tl.

Table II lists the additional parameters needed to model CsI:Tl (0.06%–0.08%), some of which did change in the process of fitting the wider array of data (i.e., the pulse shape) in this paper. The modeling in this study is done with the rate constant S_{1e} (for the electron-capture rate to form Tl^{0}) at the value measured for the nominal 0.08-mole % Tl in CsI [25], the same as the CsI:Tl fitted in Ref. [14]. Although the sample measured by Syntfeld-Kazuch and coworkers [12,13] contained 0.06-mole % Tl, we are not sure whether that falls outside the uncertainty of the nominal 0.08-wt % Tl estimate in the melt for the sample used in the picosecond measurements of S_{1e} [25].

When listing Eqs. (1)–(7) in this paper, we introduce the free-electron fraction, $f_e = U_{et}/S_{1e}$, of Tl^{0}'s that are ionized in equilibrium, so that the free-electron values of D_e, μ_e, and K_{1e} can be used in Eqs. (4)–(6) rather than defining the new parameters D_{et}, μ_{et}, and K_{1et} scaled by the same factor, as was done in Ref. [14]. The defect-trapping rate constant K_{1e} is proportional to the concentration of the responsible deep defects, which is sample dependent. Thus, a determination of K_{1e} is made in this work from fitting the decay curve of the CsI:Tl (0.06%) sample studied by Syntfeld-Kazuch *et al.* [12].

All of the changes in parameter values relative to Ref. [14] can be considered small or modest except for the two bimolecular rate constants involving thallium: B_{et} for the capture of STH on Tl^{0} and B_{tt} $(= B_{tt}^{0} f_e)$ for the capture of an electron released from Tl^{0} on Tl^{2+}, including the effect of release and recapture. The first-order-capture rate constants that had not been directly measured were estimated in Ref. [14] as the product of a cross section, the concentration of the capturing defect, and the mean velocity of approach of the mobile carrier. When the approaching mobile carrier is a self-trapped hole, the velocity of approach is quite low, governed by the STH hopping rate.

TABLE I. Parameters used for the host parameters in the CsI:Tl model of this work. Except for the deep defect-trapping rate constant K_{1e} discussed in the text, all parameters on this list are the same as those used for the calculation of proportionality and light yield in undoped CsI at 295 K in Ref. [14]. In Table I of Ref. [14], literature references for the values are listed where available; otherwise, comments on the estimation methods are listed and explained in Ref. [14]. See Ref. [14] for definitions of the parameters.

Parameter	Value	Units
r_{track}	3	nm
βE_{gap}	8.9	$(\text{eV}/e\text{-}h)_{\text{av}}$
ϵ_0	5.65	
μ_e	8	$\text{cm}^2/\text{V s}$
D_e	0.2	cm^2/s
μ_h	10^{-4}	$\text{cm}^2/\text{V s}$
D_h	2.6×10^{-6}	cm^2/s
D_E	2.6×10^{-6}	cm^2/s
$B(t > \tau_{\text{hot}})$	2.5×10^{-7}	cm^3/s
K_3	4.5×10^{-29}	cm^6/s
K_{2E}	0.8×10^{-15}	$t^{-1/2}$ cm^3 $\text{s}^{-1/2}$
R_{1E}	6.7×10^6	s^{-1}
K_{1E}	6×10^7	s^{-1}
τ_{hot}	4	ps
r_{hot} (peak)	50	nm
$D_e(t < \tau_{\text{hot}})$	3.1	cm^2/s
S_{1e}	0	s^{-1}
S_{1h}	0	s^{-1}
S_{1E}	0	s^{-1}
$G_E(r = 0)$	0	cm^{-3}
K_{1e}	2.7×10^{10}	s^{-1}
K_{1h}	$10^{-5} K_{1e}$	s^{-1}
E_i(norm)	200	keV

For capture on neutral traps (including substitutional Tl^+ in the CsI lattice), a geometrical cross section can usually be assumed without a large error. In this way, the value for S_{1h}, the first-order rate constant for the capture of STH on Tl^+, is estimated. For the second-order capture of STH on Tl^0's governed by B_{et}, the cross section is assumed to be the same as that found in picosecond absorption measurements of STH + e → STE. During fitting of the pulse shape in this work, the STH population is found to be vanishing too quickly to support the observed rise time to peak. The need for a reduced value of B_{et} becomes clear, and there is a recognition that the estimated value should take into account the low velocity of the approaching carrier (STH) in the case of $\text{STH} + \text{Tl}^0 \rightarrow \text{Tl}^{+*}$. This correction is the largest one in Table II. Because the $B_{et} n_{et} n_h$ rate term and the $S_{1h} n_h$ rate term divide the available STH population, as discussed earlier, reduction in the value of B_{et} requires a balancing decrease in the value of S_{1h}, returning it close to the value of S_{1h} originally estimated in Ref. [14]. Mainly as a result of the decrease in S_{1h}, the self-trapped holes diffuse to a larger radius before being nearly immobilized as a cylindrical positive charge of Tl^{2+}. One can compare the approximately 18-nm peak of the rn_{ht} distribution at 1 μs in Fig. 9(d) of this work to the approximately 4-nm peak of rn_{ht} at 1 μs in Fig. 10(b) of Ref. [14]. This comparison is not perfect because the plot in Ref. [14] was for a 10 times lower excitation density. In a similar comparison of rn_{et} at 1 μs in Fig. 9(d) of this work with Fig. 9(b) of Ref. [14], the 4-nm peak of rn_{et} in the earlier work is no longer seen in the corresponding 1-μs distribution of this work. This absence can be attributed mainly to the revised smaller S_{1h} hole-capture parameter causing a more diffuse distribution of Tl^{2+} (n_{ht}), which is less effective in attracting electrons to trap nearby than Tl^0 (n_{et}).

TABLE II. Additional rate constants and transport parameters used in Eqs. (4)–(6) when modeling CsI:Tl (0.06%) at 295 K in this work. S_{1e} is the value measured on CsI:Tl (nominally 0.08 mole %) [25]. See Ref. [14] for definitions of the parameters.

Parameter	Value	Units
S_{1e}	3.3×10^{11}	s^{-1}
S_{1h}	5.0×10^6	s^{-1}
S_{1E}	5.0×10^6	s^{-1}
[Tl]	0.06	mole % in sample
R_{1Et}	1.7×10^6	s^{-1}
U_{Et}	5.4×10^5	s^{-1}
B_{tt}	2.5×10^{-7}	cm^3/s
B_{et}	1.3×10^{-10}	cm^3/s
B_{ht}	2.5×10^{-7}	cm^3/s
K_{2Et}	1.7×10^{-15}	$t^{-1/2}$ cm^3 $\text{s}^{-1/2}$

The fitting of the pulse shape in this work requires a significant increase in the value of B_{tt} relative to the estimate of this second-order rate constant made in Ref. [14]. This necessity underscores a conclusion we reach in this study, that fitting the proportionality alone can be fairly forgiving on some of the parameter choices. Fitting additional data with more structure, such as multiple rise and decay components of the pulse shape, can be used to refine parameters before undertaking a calculation of proportionality, as is done in this study.

VIII. CONCLUSIONS

Recent experiments on the scintillation response of CsI:Tl [12,13] have shown that (1) there are three main decay times of about 730 ns, 3 μs, and 16 μs, i.e., one more principal decay component than had been previously reported; (2) for the sample studied, the 16-μs component appears to exhibit exponential decay, whereas the recombination kinetics widely regarded to be responsible for much of the CsI:Tl scintillation comes from second-order electron-hole recombination on the activator; (3) the pulse shape depends on gamma-ray energy; and (4) the proportionality curves of each decay component are different, with the energy-dependent light yield of the 16-μs component appearing to be anticorrelated with that of the 0.73-μs component. These observations have been reasonably explained based on the model results presented.

This model of carrier transport and recombination takes into account the most important processes of hot and thermalized carrier diffusion, electric-field transport, trapping, nonlinear quenching, and radiative recombination that can be expected to occur in particle tracks. Specifying the rates of such processes in a specific scintillator like CsI:Tl requires the assembly of a significant number of material parameter values—measured in experiments independent of scintillation when possible, calculated theoretically in some cases, and refined by fitting to properties such as scintillation decay times in a few others. The assembled parameter set, along with the equations in which the parameters appear, comprises an evolving model of scintillator response (in this study, CsI:Tl).

The following conclusions are drawn:

(1) By examining population overlaps and reaction rates within the radial profile of the track, the 3- and 16-μs components are identified as the rate- and transport-limited phases of the same basic $\mathrm{Tl}^0 + \mathrm{Tl}^{2+}$ recombination.

(2) When a recombination process (e.g., second order, in this case) becomes transport limited, depending on the electric field and the concentration gradient between two separated reservoirs of carriers, the decay kinetics become first order, consistent with the apparent exponential decay of the 16-μs tail component.

(3) The apparent exponential decay of the 730-ns fast component can be attributed mainly to the 575-ns first-order radiative decay of Tl^{+*}, but also perhaps to the finding that the 110-ns decay of the $R2$ rate feeding the Tl^{+*} is itself transport limited—and thus exponentially decaying.

(4) Results of the full model reproduce the main trend of an energy-dependent pulse shape seen in the experiment. Of the three major decay times, the 730-ns one is mainly due to $(\mathrm{STH} + \mathrm{Tl}^0)$ $R2$, in partial agreement with this attribution in the literature, but, in addition, the $(\mathrm{Tl}^0 + \mathrm{Tl}^{2+})$ $R3$ reaction at a small radius near the core contributes significantly in the time range at high excitation density (corresponding to low electron energy) and accounts for part of the energy dependence of the pulse shape.

(5) Energy transport by STE to a thallium activator can be no more than a minor contributor to any of the three main decay components at ordinary levels of Tl doping for scintillators.

(6) By analyzing the model results in terms of consumption of electrons and holes by two competing recombination reactions, second-order $R2$ and first-order Tl^{2+} formation preparatory for $R3$, we can explain why the anticorrelation of the tail and fast decay components is to be expected at room temperature. The full model that fits the three decay components of scintillation also reproduces the main features of proportionality for each of the separate decay components and is a reasonable match of the total light yield at 662 keV.

(7) When integrating the light yield to 40 μs, the calculated light output at 662 keV is 63 photons/keV, slightly higher than the reported value of 54 photons/keV [38]. However, integration for such a long time is uncommon. In the more likely measurement conditions of 12- and 4-μs integrations, the calculated yields are 57 and 48 photons/keV, which bracket the reported value.

Work is under way to model similar experimental data sets on CsI at temperatures below and above room temperature, and to model the effects of changing concentration of activators and defects. As the collection of experimental data being compared to the model expands, we anticipate further refinement of parameter values for CsI:Tl. The model and its parameters for CsI and CsI:Tl should become more comprehensive and, at the same time, more tightly specified. Important applications of such a material-validated model will be to dissect the contributing processes in space and time, as we demonstrate in this work, to gain insight on what controls various properties of the response, or to vary the concentration and the properties of activators, defects, and codopants while analyzing their contributions in ways that may not be open to direct experimental observation. Application of this basic model to other scintillator systems is under way [39–41]. A similar procedure for assembling material parameters from the literature, as well as making estimates, followed by refining against pulse shape and other data, is being employed for each scintillator system.

The present model makes certain assumptions in order to achieve relative computational simplicity. An important one is the assumption of cylindrical symmetry of track segments, rendering the problem effectively one dimensional in the radial coordinate. Kinetic Monte Carlo methods used by Kerisit *et al.* [23,24,42,43] address the local randomness of carrier distributions by simulating the individual diffusion and interactions of every electron and hole in the track starting with carrier-creation distributions simulated by the NWEGRIM code [44,45]. This approach avoids an assumption of local track symmetry but is also computationally demanding. A comparison of modeled scintillation response at energies of 400 keV and below currently addressed by both the Pacific Northwest National Laboratory (PNNL) kinetic Monte Carlo method and the Wake Forest University (WFU) transport and rate-equation method could answer questions on the effect of approximations such as cylindrical track that have enabled relatively fast simulations of scintillation response in the present work. Collaborative work of the WFU and PNNL groups is ongoing.

ACKNOWLEDGMENTS

W. F. U. acknowledges support from the U.S. Department of Homeland Security, Domestic Nuclear Detection Office, DNDO-NSF-ARI Grant No. 2014-DN-077-ARI-077 and the National Nuclear Security Administration (NNSA), Office of Defense Nuclear Nonproliferation Research and Development (DNN R&D) under Venture Contract No. LB15-V-GammaDetMater-PD2Jf through Lawrence Berkeley National Laboratory. This support does not constitute express or implied endorsement on the part of the Government. Partial support is also acknowledged from the Polish National Centre for Research and Development under the project "RaM-scaN," Grant No. PBS2/B2/11/2014 and by the European Union's Seventh Framework Programme for research, technological development, and demonstration under "TAWARA" Grant Agreement No. 312713. This work is partially supported by the NATO multiyear Science for Peace Project No. NUKR.SFPP 984958, "New sensor materials and detectors for ionizing radiation detection."

[1] Pieter Dorenbos, Fundamental limitations in the performance of Ce^{3+}, Pr^{3+}, and Eu^{2+} activated scintillators, IEEE Trans. Nucl. Sci. **57**, 1162 (2010).

[2] M. Moszyński, A. Syntfeld-Każuch, L. Swiderski, M. Grodzicka, J. Iwanowska, P. Sibczyński, and T. Szczęśniak, Energy resolution of scintillation detectors, Nucl. Instrum. Methods Phys. Res., Sect. A **805**, 25 (2016).

[3] Glenn F. Knoll, *Radiation Detection and Measurement*, 4th ed. (Wiley, New York, 2011).

[4] C. L. Melcher, Scintillators for well logging applications, Nucl. Instrum. Methods Phys. Res., Sect. B **40–41**, 1214 (1989).

[5] Nerine J. Cherepy, Steve A. Payne, Benjamin W. Sturm, Owen B. Drury, Sean P. O'Neal, Peter A. Thelin, Kanai S. Shah, Rastgo Hawrami, Michael Momayezi, Brad Hurst, Arnold Burger, Brenden Wiggins, Pijush Bhattacharya, Lynn A. Boatner, and Joanne O Ramey, Instrument development and gamma spectroscopy with strontium iodide, IEEE Trans. Nucl. Sci. **60**, 955 (2013).

[6] Paul Lecoq, Development of new scintillators for medical applications, Nucl. Instrum. Methods Phys. Res., Sect. A **809**, 130 (2016).

[7] Maurizio Conti, State of the art and challenges of time-of-flight PET, Phys. Med. **25**, 1 (2009).

[8] Paul Lecoq, Mikhael Korzhik, and Andrey Vasiliev, Can transient phenomena help improving time resolution in scintillators?, IEEE Trans. Nucl. Sci. **61**, 229 (2014).

[9] M. Moszynski, A Nassalski, A. Syntfeld-Kazuch, L Swiderski, and T. Szczecsniak, Energy resolution of scintillation detectors—New observations, IEEE Trans. Nucl. Sci. **55**, 1062 (2008).

[10] R. T. Williams, X. Lu, S. Gridin, P. Li, D. R. Onken, K. B. Ucer, A. Burger, and M. R. Mayhugh, Information on Particle Track Structure Carried in Scintillation Pulse Shape? Present and Potential Applications, in *Proceedings of the International Conference on Optical, Optoelectronic, and Photonic Materials and Applications (ICOOPMA 2016), Montreal, 2016* (unpublished).

[11] R. T. Williams, Xinfu Lu, A. Syntfeld-Kazuch, L. Świderski, M. Moszyński, and A. V. Gektin, Transport and Rate Equation Modeling of Experiments on Proportionality of Decay Time Components in CsI:Tl, in *Proceedings of the IEEE Nuclear Science Symposium and Medical Imaging Conference (NSS-MIC), San Diego, 2015* (unpublished).

[12] A. Syntfeld-Kazuch, M. Moszynski, L. Swiderski, W Klamra, and A Nassalski, Light pulse shape dependence on γ-ray energy in CsI (Tl), IEEE Trans. Nucl. Sci. **55**, 1246 (2008).

[13] Agnieszka Syntfeld-Kazuch, Lukasz Swiderski, Marek Moszynski, and Alexander V. Gektin, in *Conference Record of the IEEE Nuclear Science Symposium and Medical Imaging Conference (NSS/MIC), Seattle, 2014* (IEEE, New York, 2014), p. 1.

[14] Xinfu Lu, Qi Li, G. A. Bizarri, Kan Yang, M. R. Mayhugh, P. R. Menge, and R. T. Williams, Coupled rate and transport equations modeling proportionality of light yield in high-energy electron tracks: CsI at 295 K and 100 K; CsI:Tl at 295 K, Phys. Rev. B **92**, 115207 (2015).

[15] S. Agostinelli *et al.*, GEANT4—A simulation toolkit, Nucl. Instrum. Methods Phys. Res., Sect. A **506**, 250 (2003).

[16] Joel Q. Grim, K. B. Ucer, A. Burger, P. Bhattacharya, E. Tupitsyn, E. Rowe, V. M. Buliga, L. Trefilova, A. Gektin, G. A. Bizarri, W. W. Moses, and R. T. Williams, Nonlinear quenching of densely excited states in wide-gap solids, Phys. Rev. B **87**, 125117 (2013).

[17] L. Swiderski, R. Marcinkowski, M. Szawlowski, M. Moszynski, W. Czarnacki, A. Syntfeld-Kazuch, T. Szczesniak, G. Pausch, C. Plettner, and K. Roemer, Non-proportionality of electron response and energy resolution of Compton electrons in scintillators, IEEE Trans. Nucl. Sci. **59**, 222 (2012).

[18] M. Moszyński, M. Balcerzyk, W. Czarnacki, A. Nassalski, T. Szczęśniak, H. Kraus, V. B. Mikhailik, and I. M. Solskii, Characterization of $CaWO_4$ scintillator at room and liquid nitrogen temperatures, Nucl. Instrum. Methods Phys. Res., Sect. A **553**, 578 (2005).

[19] M. Grodzicka, M. Moszyński, T. Szczęśniak, W. Czarnacki, M. Szawłowski, Ł. Świderski, Ł. Kaźmierczak, and K. Grodzicki, Characterization of CsI:Tl at a wide temperature range (-40 °C to $+22$ °C), Nucl. Instrum. Methods Phys. Res., Sect. A **707**, 73 (2013).

[20] John D. Valentine, William W. Moses, Stephen E. Derenzo, David K. Wehe, and Glenn F. Knoll, Temperature dependence of CsI(Tl) gamma-ray excited scintillation characteristics, Nucl. Instrum. Methods Phys. Res., Sect. A **325**, 147 (1993).

[21] M. M. Hamada, F. E. Costa, M. C. C. Pereira, and S. Kubota, Dependence of scintillation characteristics in the CsI(Tl) crystal on Tl^{+} concentrations under electron and alpha particles excitations, IEEE Trans. Nucl. Sci. **48**, 1148 (2001).

[22] H. Dietrich, A. Purdy, R. Murray, and R. Williams, Kinetics of self-trapped holes in alkali-halide crystals: Experiments in NaI(Tl) and KI(Tl), Phys. Rev. B **8**, 5894 (1973).

[23] Sebastien Kerisit, Kevin M. Rosso, and Bret D. Cannon, Kinetic Monte Carlo model of scintillation mechanisms in CsI and CsI(Tl), IEEE Trans. Nucl. Sci. **55**, 1251 (2008).

[24] Zhiguo Wang, YuLong Xie, Luke W. Campbell, Fei Gao, and Sebastien Kerisit, Monte Carlo simulations of electron thermalization in alkali iodide and alkaline-earth fluoride scintillators, J. Appl. Phys. **112**, 014906 (2012).

[25] K. B. Ucer, G. Bizarri, A. Burger, A. Gektin, L. Trefilova, and R. T. Williams, Electron thermalization and trapping rates in pure and doped alkali and alkaline-earth iodide crystals studied by picosecond optical absorption, Phys. Rev. B **89**, 165112 (2014).

[26] A. Belsky, C. Dujardin, A. Gektin, S. Gridin, I. Iskandarova, A. Scherbinin, N. Shiran, and A. Vasil'ev, Activator Levels in CsI Crystals Doped with Tl^+ and In^+ Ions, in *Proceedings of the 9th International Conference on Luminescent Detectors and Transformers of Ionizing Radiation (LUMDETR 2015), Tartu, Estonia* (unpublished).

[27] V. Yakovlev, L. Trefilova, A. Meleshko, V. Alekseev, and N. Kosinov, Charge transfer processes in CsI:Tl using near-UV light, J. Lumin. **155**, 79 (2014).

[28] M. H. Du, Chemical trends of electronic and optical properties of ns^2 ions in halides, J. Mater. Chem. C **2**, 4784 (2014).

[29] V. Nagirnyi, A Stolovich, S. Zazubovich, V. Zepelin, E. Mihokova, E. Nikl, G. P. Pazzi, and L Salvini, Peculiarities of the triplet relaxed excited-state structure and luminescence of a CsI:Tl crystal, J. Phys. Condens. Matter **7**, 3637 (1995).

[30] R. Gwin and R. Murray, Scintillation process in CsI(Tl). II. Emission spectra and the possible role of self-trapped holes, Phys. Rev. **131**, 508 (1963).

[31] Shunji Nagata, Koji Fujiwara, and Hitoshi Nishimura, Dynamical aspects of excitons in NaI, J. Lumin. **47**, 147 (1990).

[32] H. Nishimura, M. Sakata, T. Tsujimoto, and M. Nakayama, Origin of the 4.1 eV luminescence in pure CsI scintillator, Phys. Rev. B **51**, 2167 (1995).

[33] Lukasz Swiderski, Marek Moszynski, Antoni Nassalski, Agnieszka Syntfeld-Kazuch, Wieslaw Czarnacki, Wlodzimierz Klamra, and Valentin A. Kozlov, Scintillation properties of undoped CsI and CsI doped with CsBr, IEEE Trans. Nucl. Sci. **55**, 1241 (2008).

[34] Lukasz Swiderski, Marek Moszynski, Agnieszka Syntfeld-Kazuch, Marek Szawlowski, and Tomasz Szczesniak, Measuring the scintillation decay time for different energy depositions in NaI:Tl, LSO:Ce and $CeBr_3$ scintillators, Nucl. Instrum. Methods Phys. Res., Sect. A **749**, 68 (2014).

[35] R. Murray and A Meyer, Scintillation response of activated inorganic crystals to various charged particles, Phys. Rev. **122**, 815 (1961).

[36] S. Gridin, A. Belsky, C. Dujardin, A. Gektin, N. Shiran, and A. Vasil'ev, Kinetic model of energy relaxation in CsI:A ($A = Tl$ amd In) scintillators, J. Phys. Chem. C **119**, 20578 (2015).

[37] Zhiguo Wang, YuLong Xie, Bret D. Cannon, Luke W. Campbell, Fei Gao, and Sebastien Kerisit, Computer simulation of electron thermalization in CsI and CsI(Tl), J. Appl. Phys. **110**, 064903 (2011).

[38] See http://www.crystals.saint-gobain.com.

[39] M. R. Mayhugh, Xinfu Lu, S. Gridin, S. B. Donnald, C. L. Melcher, and R. T. Williams, From CsI:Tl to YAP:Ce—A Modeling Study of the Material Parameter Sensitivity of Proportionality, in *Proceedings of the Symposium on Radiation Monitoring and Applications (SORMA West 2016), Berkeley, 2016* (unpublished).

[40] K. B. Ucer, Sergii Gridin, Peiyun Li, Xinfu Lu, R. T. Williams, M. R. Mayhugh, A. V. Gektin, Kan Yang, P. R. Menge, and G. A. Bizarri, NaI and NaI:Tl Picosecond Spectroscopy and Scintillation Modeling, in *Proceedings of the Symposium on Radiation Monitoring and Applications (SORMA West 2016), Berkeley, 2016* (unpublished).

[41] S. Gridin, X. Lu, P. Li, B. Ucer, R. Williams, K. Yang, and P. Menge, $LaBr_3$ with Ce and Sr Dopants: Picosecond Absorption Spectroscopy and Progress on Track Modeling, in *Proceedings of the International Conference on Defects in Insulating Materials (ICDIM 2016), Lyon, France* (unpublished).

[42] Sebastien Kerisit, Kevin M. Rosso, Bret D. Cannon, Fei Gao, and YuLong Xie, Computer simulation of the light yield nonlinearity of inorganic scintillators, J. Appl. Phys. **105**, 114915 (2009).

[43] Zhiguo Wang, Richard T. Williams, Joel Q. Grim, Fei Gao, and Sebastien Kerisit, Kinetic Monte Carlo simulations of excitation density dependent scintillation in CsI and CsI(Tl), Phys. Status Solidi (b) **250**, 1532 (2013).

[44] Fei Gao, Luke W. Campbell, Ram Devanathan, Yulong Xie, L. Rene Corrales, Anthony J. Peurrung, and William J. Weber, Monte Carlo method for simulating γ-ray interaction with materials: A case study on Si, Nucl. Instrum. Methods Phys. Res., Sect. A **579**, 292 (2007).

[45] F. Gao, Y. Xie, S. Kerisit, L. W. Campbell, and W. J. Weber, Yield, variance and spatial distribution of electron-hole pairs in CsI, Nucl. Instrum. Methods Phys. Res., Sect. A **652**, 564 (2011).